SANDIA REPORT

SAND2018-10707
UUR
Printed September 2018

Big-Data Multi-Energy Iterative Volumetric Reconstruction Methods for As-Built Validation & Verification Applications

Edward S. Jimenez

Prepared by
Sandia National Laboratories
Albuquerque, New Mexico 87185 and Livermore, California 94550

Sandia National Laboratories is a multimission laboratory managed and operated by National Technology and Engineering Solutions of Sandia, LLC, a wholly owned subsidiary of Honeywell International, Inc., for the U.S. Department of Energy's National Nuclear Security Administration under contract DE-NA0003525.

Sandia National Laboratories

Issued by Sandia National Laboratories, operated for the United States Department of Energy by National Technology and Engineering Solutions of Sandia, LLC.

Available to DOE and DOE contractors from
U.S. Department of Energy
Office of Scientific and Technical Information
P.O. Box 62
Oak Ridge, TN 37831

Telephone: (865) 576-8401
Facsimile: (865) 576-5728
E-Mail: reports@adonis.osti.gov
Online ordering: http://www.osti.gov/bridge

Available to the public from
U.S. Department of Commerce
National Technical Information Service
5285 Port Royal Rd
Springfield, VA 22161

Telephone: (800) 553-6847
Facsimile: (703) 605-6900
E-Mail: orders@ntis.fedworld.gov
Online ordering: http://www.ntis.gov/help/ordermethods.asp?loc=7-4-0#online

SAND2018-10707
UUR
Printed September 2018

Big-Data Multi-Energy Iterative Volumetric Reconstruction Methods for As-Built Validation & Verification Applications

Edward S. Jimenez

Abstract

This document archives the results developed by the Lab Directed Research and Development (LDRD) project sponsored by Sandia National Laboratories (SNL). In this work, it is shown that SNL has developed the first known high-energy hyperspectral computed tomography system for industrial and security applications. The main results gained from this work include dramatic beam-hardening artifact reduction by using the hyperspectral reconstruction as a bandpass filter without the need for any other computation or pre-processing; additionally, this work demonstrated the ability to use supervised and unsupervised learning methods on the hyperspectral reconstruction data for the application of materials characterization and identification which is not possible using traditional computed tomography systems or approaches.

Contents

List of Figures

List of Tables

Chapter 1

Original Proposal

Overview

Project Purpose

Identifying slight nuances of as-built components is important in simulating dynamic systems such as explosive reactions. These systems are inherently chaotic; slight input deviations may create large changes in a given simulation. This problem is realized in the performance of idealized component models versus that of as-built components. Strict tolerances are needed to ensure optimal performance; defects and imperfections cause degradation or failure. SNLs computational tools, such as SIERRA and CTH, simulate these systems; however, inaccurate 3D experimental characterization introduces input errors that potentially generate significant computational errors. Currently, 3D physical data generation uses computed-tomography (CT). CT is suboptimal in supporting segmentation of components with contrasting materials such as foam juxtaposed with metal due to artifacts and noise at the boundaries and interfaces. Instead, we propose a Multi-Energy Iterative Reconstruction (MEIR) method that produces superior volume reconstructions from x-ray images and improved materials identification through values proportional to elemental composition. The challenge in MEIR is the immense computational complexity (5th-order scaling in voxels). Furthermore, engineering datasets are six orders-of-magnitude larger than medical CT datasets, which is where current experience concentrates. MEIR will fundamentally change experimentation and simulation validation at Sandia, enabling identification of defect influence in modeling. Improved ability to inspect, diagnose, and identify objects of interest directly leads to increased confidence levels of design, reliability, and assessment. Our goal is to produce substantially higher-quality images compared to traditional CT and segment components of interest suitable for CTH and SIERRA so that computational simulations can be executed.

Why is this proposed as an LDRD Project?

- Big-data MEIR has not been attempted due to risk related to the immense post-processing.

- The proposed novel acquisition technique explores nascent technology (with its own nontrivial risks) that potentially revolutionizes SNLs advanced diagnostics and Non-destructive Testing (NDT) capabilities.

- If both succeed, then they transform NDT, big-data science, advanced diagnostics, information management for SNL engineering applications, and SNLs world-class radiography capabilities.

Proposed R&D

Technical Approach and Leading Edge Nature of Work

Our proposed MEIR method implements a hybrid massively-multithreaded approach using GPUs and dynamically adapts itself to problem scope such as methods similar to [23]. Utilization of GPUs will reduce computational time for calculations thus creating a feasible approach. Traditionally, to achieve improved reconstruction quality without significantly increasing post-processing time, one would turn to dual-energy radiography (DER). DER is frequently used to simplify/clarify the complex visual field created by radiographs [14] as well as to detect broad classes of materials [31]. Although the computational burden increases minimally, the imaged object is subjected to approximately twice the radiation dose and scan time. Doubling dose and time is restricting as many sensitive components can be damaged from the additional dose and thus are not candidates for DER. DER has severe limitations due to the non-linear behavior of x-ray imaging systems and polychromatic nature of most x-ray sources thus limiting its capabilities, especially in material classification; Jimenez et. al. showed this [26, 24, 22, 27] while exploring alternatives to DER. In medicine, iterative reconstruction is used to produce superior reconstructions that contain fewer artifacts compared to standard technologies while simultaneously reducing dose. Iterative solutions will yield higher-quality volumetric approximations than direct methods by reducing artefacts due to acquisition deficiencies such as photon starvation, beam hardening, and under-sampling[19, 5]. The main drawback is the non-negligible added computation and the lack of scalability to industrial datasets where the data can be up to six orders-of-magnitude larger [23, 21]; hence, the need for an innovative irregular (i.e. non-deterministic data access patterns) approach for big-data. Iterative methods fundamentally differ from methods utilized by SNL by simulating non-linearities of imaging systems accurately [8]. To successfully implement MEIR, the core work will revolve around addressing the big data problem unique to imaging system simulation and reconstruction. Forward- and Back-projection algorithms operating on big data, significantly exceeding 10 GB, in a massively parallel environment will suffer from performance degradation due to the non-deterministic memory/information access pattern by the collection of computational threads [23, 35]. Adding more computational resources will actually slow the computation due to the increased data traffic, exacerbating data starvation. Irregular algorithms such as [23] reduce latencies in the computation by optimizing information movement locally and globally; thus improving computational time

and energy efficiency, therefore allowing the task to be completed with fewer resources. Additionally, this work will investigate data acquisition techniques. Many acquisition techniques in the scientific literature focus on human body parts and shapes which differ with those relevant to engineering applications (i.e. flat objects, torus shaped objects, tubular, etc.). This effort is dual-use, not only does this investigation provide optimal scanning patterns for quality projection data, but will ideally reduce dose to the scanned component, both of which are of great importance to SNL and advanced diagnostics in general. Finally, once MEIR prototypes are developed (forward-projection, back-projection, filtering, etc.), this work will extend those prototypes to realistic and mission critical imaging datasets such as shape charges, detonators, and batteries to determine the ultimate success of this work Overall, a key goal is to combine the best features of multi-energy radiography with the superior qualities of iterative reconstruction algorithms at industrial scales of up to 1 trillion voxels to deliver a revolutionary advanced diagnostics tool. To achieve this, there are many challenges that must be addressed:

- Designing the novel big-data centric Landweber-type iterative reconstruction algorithm [2].
- Investigate non-traditional data acquisition techniques that optimize data quality for shapes relevant to engineering applications (i.e. planar, tubular, torus, etc.).
- Experimentation with algorithm design and its impact on GPU performance (Partitioning, synchronization, load balancing, and reuse of data [25]).
- Developing approaches to local noise suppression that induce bounded global noise.
- Investigate sampling techniques with respect to spectral energy and position to improve data quality. MEIR would require modest COTS hardware, thereby reducing cost/complexity while exhibiting scalability, and enabling diagnostic processing of relevant data sets within hours.

Iterative methods in radiography typically require less radiation exposure, minimizing impact on components by reducing the number of projections necessary and maximizing the x-ray data utilization [5], an important advantage for SNL imaging applications. Both small and large-scale datasets will be used to ensure that performance is scalable and flexible. Experimental data will consist of CT datasets acquired using multiple energy spectrums in various relevant configurations. The objects scanned will be representative of objects of mission interest to SNL having sufficient complexity to test and evaluate both the performance of the reconstruction algorithm and derived ability to segment the subcomponents within the object. Summary technical goals that address the research challenges identified above are:

- Deliver improved advanced diagnostics that execute on diverse computing platforms.
- Reconstruct datasets from 1 gigavoxel to 1 teravoxel in size within 24 hours with modest resources.

- The algorithms will exhibit energy efficiency and not require extraordinary power sources.
- Demonstrate superior subcomponent segmentation on an as-built component compared to CT.
- Develop a novel acquisition technique that minimizes dose and acquisition time while enabling MEIR.

MEIR would be the first iterative-type algorithm targeted at engineering big-data and industrial applications, and thus would position Sandia as a leader in this important and high-impact technology. This is a crucial tool for many applications of interest to SNL, particularly as an additive manufacturing diagnostic that steps significantly beyond currently applied CT technology. Patents and scientific papers are expected from this research and will be produced appropriately.

Relationship to Prior and Other On-Going Work

- Prior work done by members of this LDRD team leverages polychromatic information of incident x-ray energy to obtain superior material identification capabilities using x-ray. This work was a highly exploratory approach funded by an LDRD [26, 24, 22, 27] and can potentially be exploited in a volumetric reconstruction that surpasses DER methods [14].
- Prior work by the PI (Early Career LDRD) addressed the challenges of big data reconstruction for traditional CT. This work was the first to pose big data industrial CT as an irregular problem and addressed it by developing a new approach that was not only scalable from a laptop to a heterogeneous cluster, but was also up to 2000 times faster and up to 35 times more energy efficient [23, 21, 25]. A preliminary study was done to investigate the challenges of the forward projection problem (a necessary subcomponent for Landweber algorithms) for big data. The results identified some of the challenges that will help steer the investigation of this proposed R&D [35].
- This work is fundamentally different than past SNL efforts in CT for complicated engineering data sets, and rests on maturation of iterative image processing methods.

Chapter 2

Comparing Imaging Capabilities of Multi-Channel Detectors to Traditional X-Ray Detector Technology for Industrial and Security Applications

Summary

This work will investigate the imaging capabilities of the Multix multi-channel linear array detector and its potential suitability for big-data industrial and security applications versus that which is currently deployed. Multi-channel imaging data holds huge promise in not only finer resolution in materials classification, but also in materials identification and elevated data quality for various radiography and computed tomography applications. The potential pitfall is the signal quality contained within individual channels as well as the required exposure and acquisition time necessary to obtain images comparable to those of traditional configurations. This work will present results of these detector technologies as they pertain to a subset of materials of interest to the industrial and security communities; namely, water, copper, lead, polyethylene, and tin.

Introduction

The objective of this work is to create a color X-ray Radiography and Computed Tomography (CT) capability at Sandia National Laboratories for R&D in industrial, security, and general non-destructive testing applications at almost arbitrary scale and configuration. Also known as Energy-Discriminated or Energy-Resolved Imaging, the potential applications that are relevant to Sandia National Laboratories Multi-Mission environment include verification & validation, high-magnification/high-energy CT, quality assurance, anomaly/target detection, checkpoint security, material identification, and real-time multi-energy CT. It is well known that traditional CT approaches that utilize Bremsstrahlung radiation sources

undoubtedly will contain some level of artifacts, noise, or both due to beam-hardening, which is caused by the non-linear preferential absorption of lower energy X-rays compared to the high energy X-rays which leads to an increase in the average energy incident on the X-ray detector versus the average energy incident on the object. Many of these artifacts could potentially be mitigated by pre-hardening or post-hardening the radiation before the radiation impinges the detector; however, this does not completely eliminate the noise or adequately address the challenge. Furthermore, hardening of the radiation may cause additional issues such as, reducing contrast of the lower attenuating materials, introduce additional scatter due to the hardening filter, as well as potentially increase scan time due to the reduction in photon flux at the detector. Other applications that could benefit from energy-discriminated/Resolved imaging includes materials classification/identification such as that done by Jimenez et. Al.[24], Collins et. Al.[7], and Wurtz et. Al.[39] in which dual-energy or multi-energy approaches could potentially be improved by leveraging the energy-resolved data. Energy-resolved imaging has already been demonstrated to show great promise in the medical community such as in Dual-energy Radiography,4 and in the detection of neoplastics in breast tissue by Johns and Yaffe[29].

Background

This work will demonstrate the performance of an energy-resolved linear array that was recently acquired and utilize two potential applications as an indicator of potential performance. The two applications will be that of attenuation profile with respect to energy estimation investigated by Collins et. Al.[7] and Jimenez et. Al.[24, 22, 27] and the work done at Lawrence Livermore National Laboratory (LLNL) by Wurtz et. Al.[39] with the LLNL-Metric for materials classification.

Although other applications were mentioned above as other examples that could potentially be improved by energy-resolved imaging, they were not considered in this work as they require additional hardware such as staging systems and other hardware that has not been integrated into the imaging system that is currently under assembly at the time of this work. One the required hardware has been integrated, a follow-up effort will be reported.

Materials Identification

Work done by Collins et. Al.[7] to verify approaches proposed by Jimenez et. Al.[24, 22, 27] presented an experimental approach to acquire X-ray transmission data from a single pixel Cadmium-Telluride (CdTe) detector creating over one thousand channels of binned X-ray energy data for energies up to 450keV. Although this preliminary work showed that further work much be conducted; much promise was shown by demonstrating that the characteristic K-edges in the attenuation profile can be extracted for some of the materials of interest.

Collins et. Al. attempt two methods of extracting the attenuation profile with respect

to energy, the first is a direct calculation based on Beers Law, the detector reading without material present between the source and detector, and a detector reading with the material of interest present. Although it was expected to encounter challenges due to noise for the low-end channels and pulse pile-up for the high-end channels, Collins et. Al. were able to resolve the K-edges for some materials as was demonstrated by the numerical simulations performed by Jimenez et. Al.

LLNL-Metric

2.2 LLNL-Metric Wurtz et. Al. at Lawrence Livermore National Laboratory proposed a dual-energy metric that does not depend on the imaging system geometry or material/sample thickness to classify materials of interest for cargo screening applications.3 This evolution on dual-energy Radiography methods measures:

$$\left(\frac{\frac{I}{I_0}|_l}{\frac{I}{I_0}|_h}, \quad ln\left(\frac{I}{I_0}|_l \right) \right),$$

where $\frac{I}{I_0}|_l$ is an image ratio of a light image and object present image at a low-energy setting and similarly, $\frac{I}{I_0}|_h$ is the same ratio acquired at some higher energy setting. This example is being used as a performance metric as energy-resolved imaging can directly integrate the LLNL-Metric by using single channels or sums of subsets of channels to create high and low-energy reading for I and I_0; thus allowing a potentially faster, simpler, or more efficient acquisition to take place as well as with potentially lower dose as only a single energy resolved measurement is required.

Approach

This work proposes using energy-resolved imaging to improve various data quality issues in traditional X-ray Radiography and CT methods. Given energy-resolved images, one can leverage the individual binned channel data to effectively achieve almost mono-energetic image data that is beyond the capabilities of any filtering configuration on a Bremsstrahlung source, reject noisy bins/regions, and potentially reduce dose and scan-time. Although these methods have already benefited various medical applications as mentioned above; they have not been necessarily proven for industrial and security applications.

Experimental Design

This work will demonstrate performance of the recently acquired Multix Detection ME100 detector using a 450kVP Comet X-ray Source as well as 5 sheets of materials of interest: Tin with a thickness of 0.813mm, Copper with a thickness of 0.2mm, Lead with a thickness

of 0.76mm, Polyethylene with a thickness of 13.5mm, and Water in a plastic container with a thickness of 59.2mm. These materials were chosen as the work by Jimenez et. al.[24] focused on these materials while Collins et. al.[7] focused on the first three. The Multix Detector consists of 5 modules, each with 128 pixels for a total of 640 pixels. The modules are arranged side-by-side to form a linear array approximately 0.5 meters wide with module pixels having a 0.8mm pixel pitch, adjacent pixels on different modules have a wider pitch that is currently unknown to the authors of this work. According to the documentation, each pixel in the ME100 module is capable of binning data into 128 channels which span a 300keV energy window with each channel uniformly spaced across the energy window. Each pixel can handle up to 1M counts per second. Many settings typical to energy resolved detectors are fixed by the manufacturer such as gain; other information, such as dead-time/live-time are not reported by the hardware. It is unknown to the authors whether the ME100 modules perform any type of scatter rejection, correction, or calibration and wish to gain insights to these questions with our measurements. As the imaging system is still under construction, only line readings (as opposed to full 2D images) will be acquired; the geometry of the system was made to replicate the geometry that Collins et. Al. utilized and will compare results from this work to those of Collins et. Al. when possible. The data acquisition will vary the x-ray source energy settings from 50 to 300keV in 50keV increments and will test multiple currents for each measurement and will have a constant exposure time of 1 second. This work will measure detector count rate scalability across current and energy, performance on the Collins et. Al. direct calculation for each of the materials listed above, performance of the LLNL-Metric for each of the materials of interest, measurement of the mean spectrum output across pixels for each of the materials of interest as well as through air, measurement of normalized spectra at each energy for various currents, and measurement of signal-to-noise with respect to both energy channel and pixel position.

Count Rate

Count rates of the Energy Resolved Detector (ERD) at various energies and currents are shown in figs. figs. 2.1 to 2.6. Each of these plots have a zero-intercept line and general line fit to the data to show the scalability with respect to current. Each data point is a sum of all pixel counts across the 640 pixel araray; all energies show good scalability as current is varied as well as no sign of saturation.

Direct Calculation

5.2 Direct Calculation Direct estimates the the attenuation profile with respect to energy from Multix detector data are shown in figs. figs. 2.7 to 2.9 respectively. Direct estimates of the attenuation profile from Multix Detector data are shown next to the Amptek detector estimates performed by Collins et. Al.[7] for Copper and Tin in figs. figs. 2.10 and 2.11 respectively. It is clear from fig. fig. 2.7 that it is indeed possible to estimate the characteristic K-edges of materials as was shown in Jimenez et. Al.[24] and Collins et. Al.; however, from

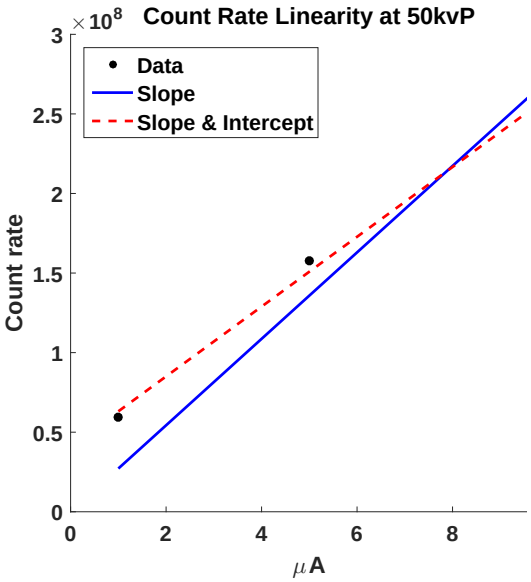

Figure 2.1: Count Rate of the ERD at 50kVP.

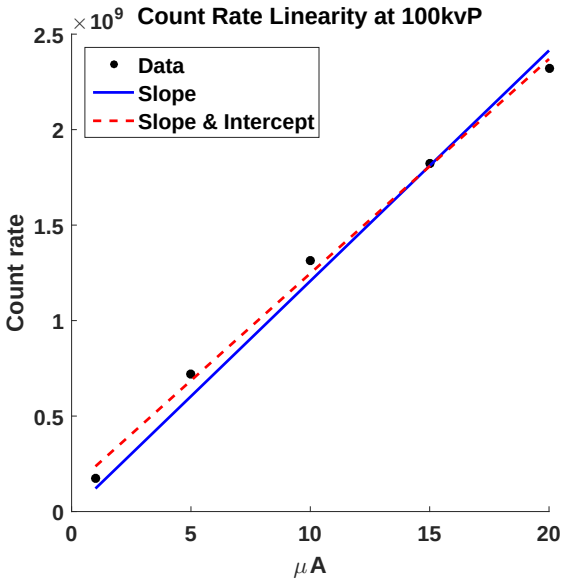

Figure 2.2: Count Rate of the ERD at 100kVP.

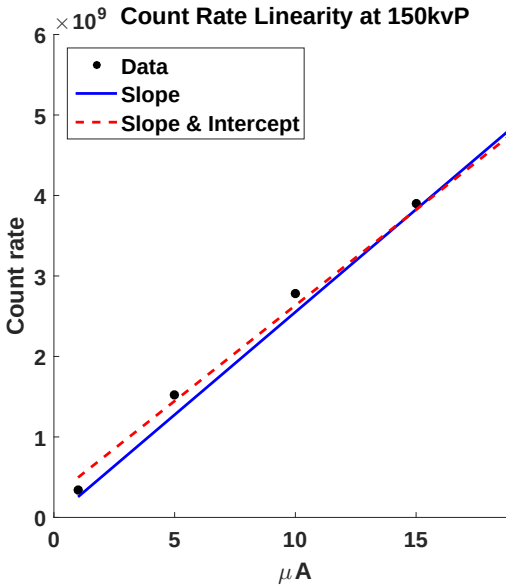

Figure 2.3: Count Rate of the Energy Resolved Detector at 150kVP.

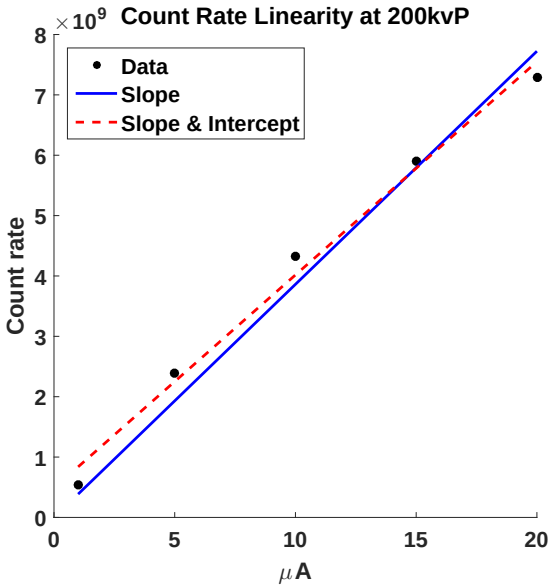

Figure 2.4: Count Rate of the Energy Resolved Detector at 50kVP.

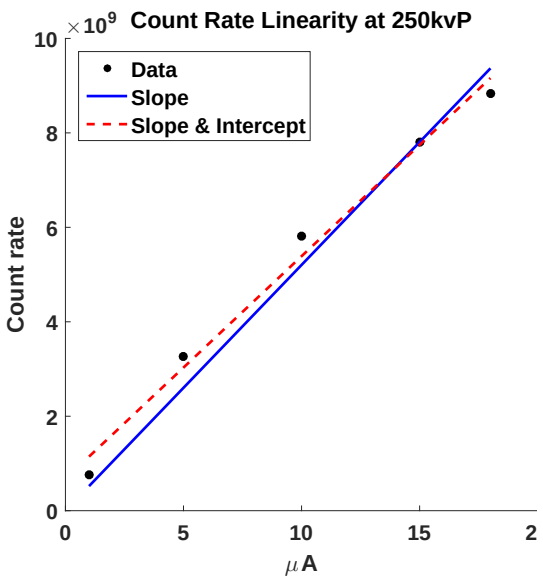

Figure 2.5: Count Rate of the Energy Resolved Detector at 250kVP.

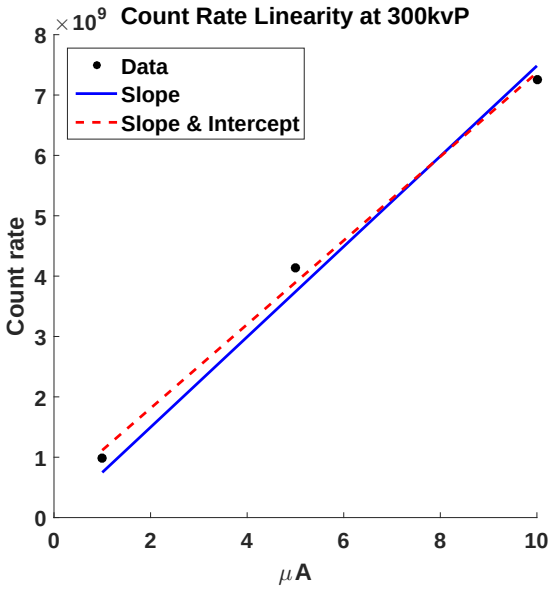

Figure 2.6: Count Rate of the Energy Resolved Detector at 300kVP.

figs. figs. 2.10 and 2.11, there is clearly some corrections that need to be made to the Multix raw data as the estimates seem to be very inaccurate when compared to the estimates of Collins et. Al.

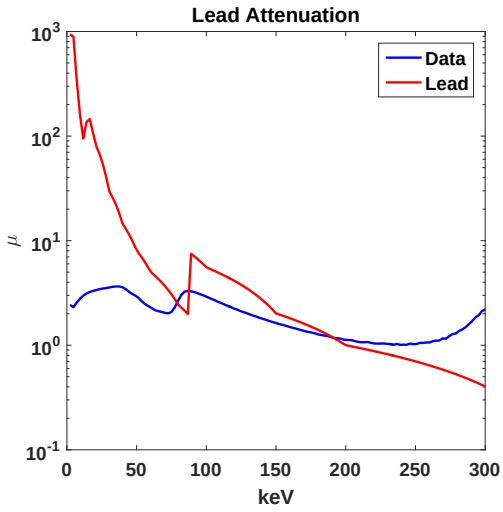

Figure 2.7: Direct estimate of the attenuation profile for Lead at 300kVP from the Energy Resolved Detector.

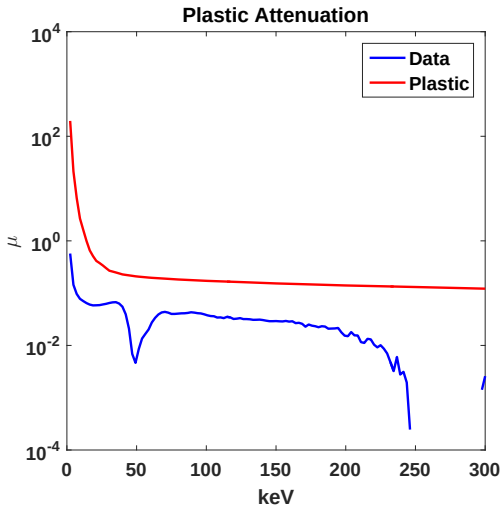

Figure 2.8: Direct estimate of the attenuation profile for Polyethylene at 300kVP from the Energy Resolved Detector.

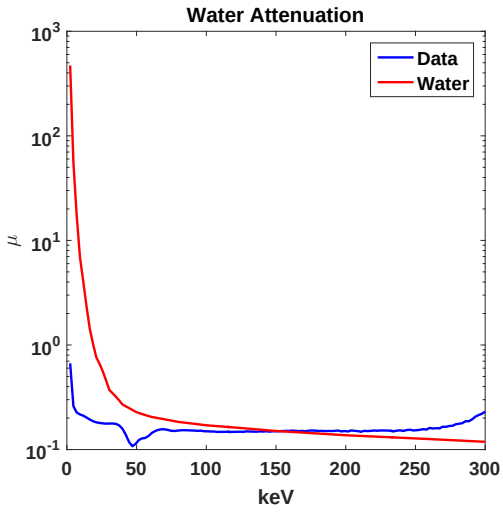

Figure 2.9: Direct estimate of the attenuation profile for Water at 300kVP from the Energy Resolved Detector.

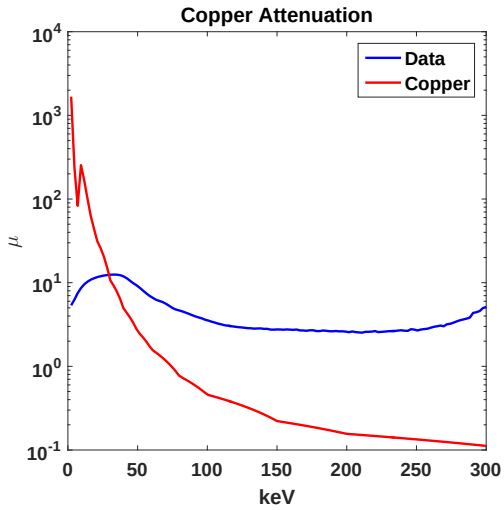

Figure 2.10: Direct estimate of the attenuation profile for Coppper at 300kVP from the Energy Resolved Detector.

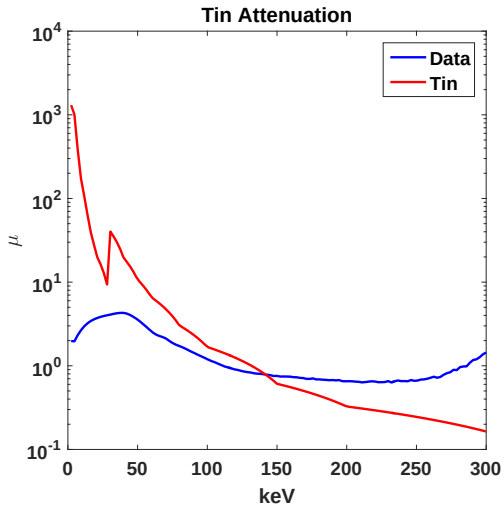

Figure 2.11: Direct estimate of the attenuation profile for Tin at 300kVP from the Energy Resolved Detector.

Lawrence Livermore National Laboratory Metric

The LLNL-Metric is shown in figs. figs. 2.12 and 2.13. The plot shown in fig. fig. 2.12, is the traditional visualization of the metric with fig. fig. 2.13 being another visualization to show how the metric various as the higher energy is varied; in this case, the lower energy was selected to be the channel that corresponds to the 150keV energy bin and every other bin with higher energy was used to calculate various metrics using various high energies. For the given thicknesses, Multix data seems to show very good separation between materials when plotted in the traditional manner. Further work is needed to study variations with respect to thickness to completely determine its viability.

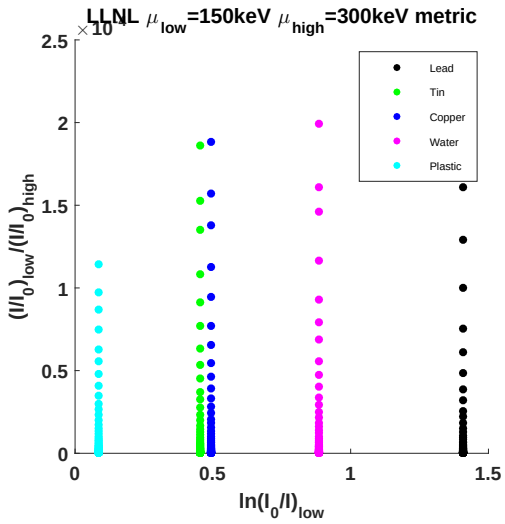

Figure 2.12: Performance of the LLNL Metric for varying keV with 5 materials using the Energy Resolved Detector.

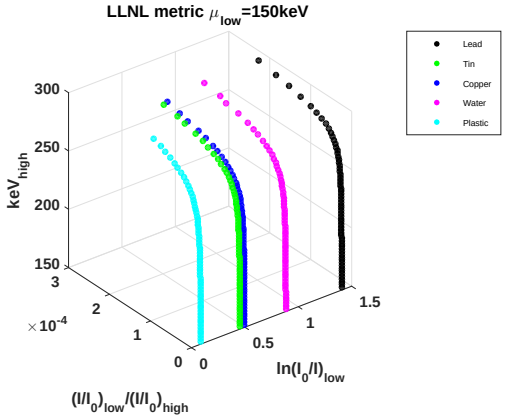

Figure 2.13: A 3D view of the performance of the LLNL Metric for varying keV with 5 materials.

Mean Spectrum Output

The mean spectrum output for the materials of interest is shown in fig. 2.14. The characteristic peak for Tungsten is visible for the less attenuative materials and dissipates for the higher attenuative materials with signs of potential noise as Water and Lead seem to show comparable attenuating properties for 200-250keV.

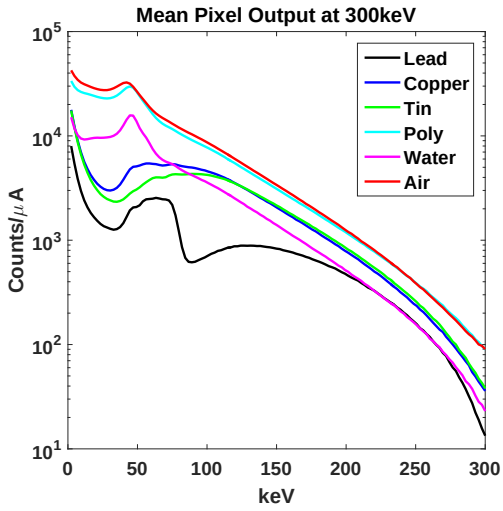

Figure 2.14: Mean pixel output with respect to energy bin for 5 different materials at 300 kVP.

Normalized Spectra

Normalized Spectra at 50keV increments are shown in figs. figs. 2.15 to 2.20 for various current settings. For the figures corresponding to settings below 300kVP, it is clear that there is significant pulse pile-up in the data by the presence of counts above the settings for each acquisition as well as an under-representation of the low energy counts; ideally, for some reasonable current settings, when the spectra is normalized, each profile regardless of current setting should overlap with all profiles corresponding to the same kVP setting.

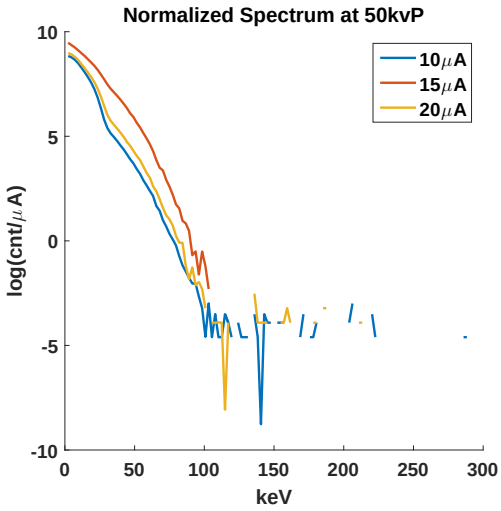

Figure 2.15: Normalized unfiltered spectra at 50 kVP for varying currents.

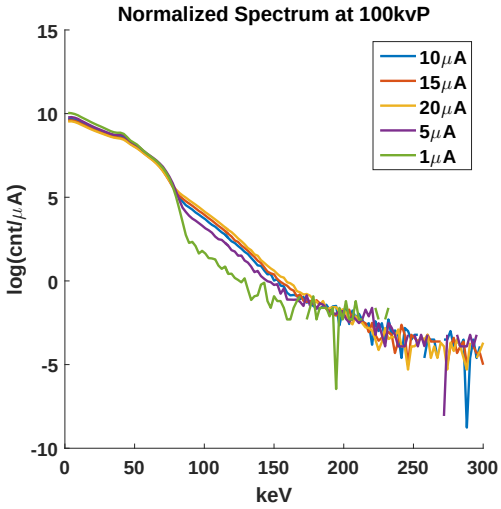

Figure 2.16: Normalized unfiltered spectra at 100 kVP for varying currents.

Signal-to-Noise

Signal-to-Noise with respect to pixel position is shown in fig. 2.21. The pixel SNR appears to be consistent across position; there appears to be a cyclical nature to the SNR, but more investigation is needed to find the cause. SNR with respect to energy is shown in fig. 2.22 and shows acceptable levels across a majority of the energy window with the best SNR being achieved for energies between 50-250keV and is possibly mostly due to noise in the system as well as pile-up.

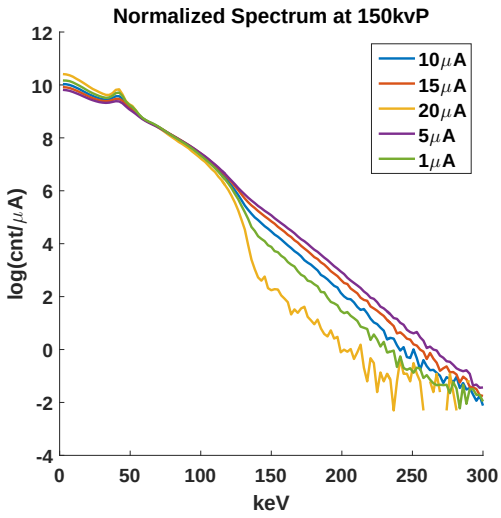

Figure 2.17: Normalized unfiltered spectra at 150 kVP for varying currents.

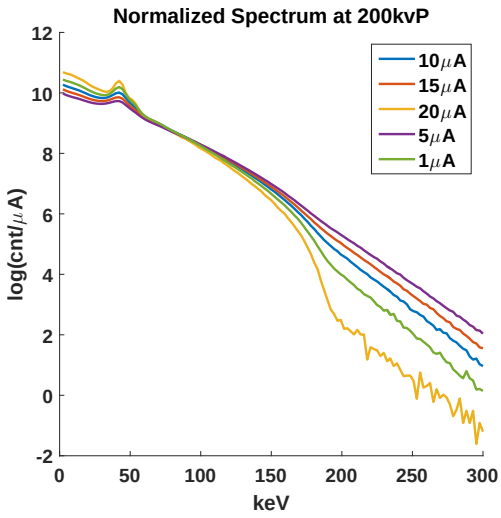

Figure 2.18: Normalized unfiltered spectra at 200 kVP for varying currents.

Conclusions

This work has demonstrated early performance metrics with the Multix energy discriminating linear array and its potential viability as an R&D Non-Destructive Evaluation imaging system. While there is much work to be done to investigate its full sensitivities as well as develop calibration and correction methods; the system holds promise in pushing the boundaries of technology and capabilities not just for Sandia National Laboratories, but for the entire Industrial and Security Non-Destructive Evaluation community. While many works have shown methods to spectrum correction,810 it still needs to be investigated whether new approaches need to be developed for applications in the higher energy ranges. The utilization and integration of energy-resolved x-ray imaging will have and has already demonstrated widespread impact; work leveraging this technology includes Johns and Yaffe,5 Tomita et.

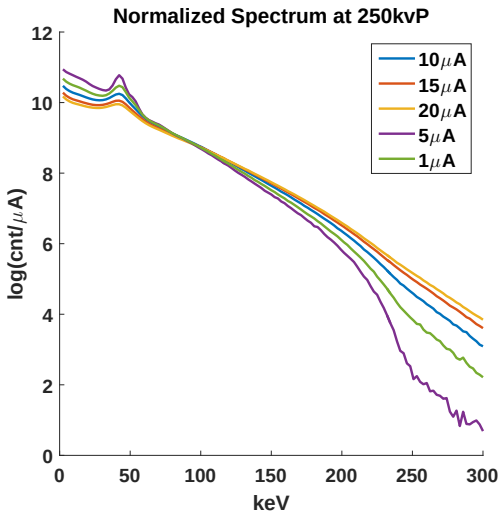

Figure 2.19: Normalized unfiltered spectra at 250 kVP for varying currents.

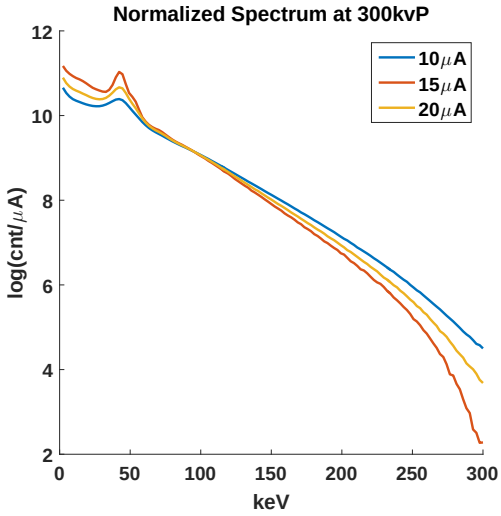

Figure 2.20: Normalized unfiltered spectra at 300 kVP for varying currents.

Al.,11 Jimenez et. Al.[24] and Collins et. Al[7].Additionally, this technology could impact other works that are based on Dual-energy approaches such as the works [39, 4, 36].

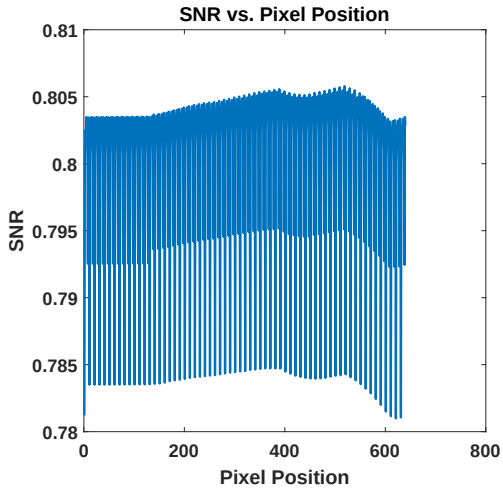

Figure 2.21: Signal-to-Noise ratio with respect to pixel position from the Energy Resolved Detector at 300 kVP.

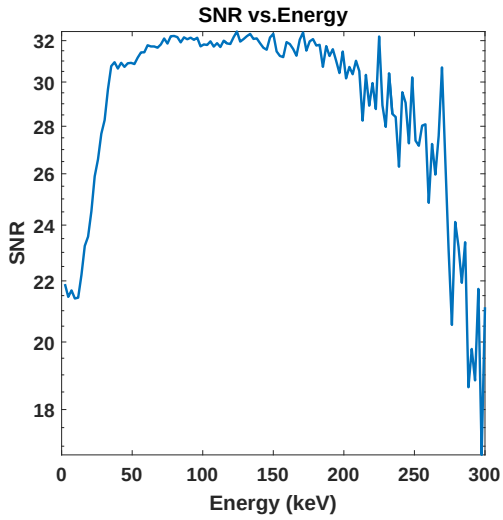

Figure 2.22: Signal-to-Noise ratio with respect to energy bin from the Energy Resolved Detector at 300 kVP.

Chapter 3

Leveraging Multi-Channel X-Ray Detector Technology to Improve Quality Metrics for Industrial and Security Applications

Summary

Sandia National Laboratories has recently developed the capability to acquire multi-channel radiographs for multiple research and development applications in industry and security. This capability allows for the acquisition of x-ray radiographs or sinogram data to be acquired at up to 300 keV with up to 128 channels per pixel. This work will investigate whether multiple quality metrics for computed tomography can actually benefit from binned projection data compared to traditionally acquired grayscale sinogram data. Features and metrics to be evaluated include the ability to distinguish between two different materials with similar absorption properties, artifact reduction, and signal-to-noise for both raw data and reconstructed volumetric data. The impact of this technology to non-destructive evaluation, national security, and industry is wide-ranging and has to potential to improve upon many inspection methods such as dual-energy methods, material identification, object segmentation, and computer vision on radiographs.

Introduction

This work is an expansion of the work presented by Jimenez et. al. [20], which describes how Sandia National Laboratories is developing a color X-ray Radiography and Computed Tomography (CT) capability for research and development applications in industrial, security, and general non-destructive testing applications. This work is the culmination of exploratory efforts in extracting more information from energy-resolved imaging applications such as that presented by Collins et. al. [7], and multiple works by Jimenez et. al. [22, 27, 24].

It is well known that traditional Computed Tomography acquisition methods using Bremsstrahlung radiation sources have several limitations that create lower-fidelity information; examples include reconstruction artifacts due to beam-hardening, streaking artifacts due to lack of penetration power, and limited ability to execute precise materials classification tasks. Some of these limitations can be somewhat mitigated using additional computational methods [39] or dual-energy approaches [4, 15], but results in extra processing and/or data acquisition.

Energy-resolved x-ray information could potentially lead to new solutions that could create better quality reconstructions or lead to more information being extracted from a given pixel in a radiograph or voxel in a computed tomography reconstruction. Previous work by Jimenez et. al. [20] focused on radiography capabilities showing that potential exists, but the data acquired is noisy, leading to some limitations. In this work, the authors will focus on energy-resolved computed tomography and its application improving image quality and artifact reduction.

Background

The Color CT system at Sandia National Laboratories consists of five customized Multix ME100 modules calibrated for 300 keV across 128 channels configured into a linear array for a total of 640 pixels across a 0.5m field-of-view, four axis motion control (one rotary, three translation), and a Comet x-ray source capable of up to 450keV/20uA. The system has a source-to-detector distance of approximately 2.06m and variable source-to-object distance. In the near future, a second vertical axis will be added to the detector to allow for an effective scan height of approximately 2.75m; up from its current vertical travel of approximately 1.4m.

The system has been acquiring data since May 2016 with sinogram acquisition capability added May 2017. Figure 3.1 shows sinogram data for channels 0, 63, and 127 for a given CT scan. Like many x-ray energy-resolved applications, the main limitation will be the noise content of the system as photon-starvation in the individual channels as well as noise from issues such as pulse pile-up, scatter, and spectral drift could become an issue.

There are many motivating factors to developing a high-energy color CT capability. Until recently, this technology was largely infeasible for all industrial x-ray imaging and CT applications. Infeasibility was due to various factors such as size, cost, acquisition time, and dataset size. However, many of these limitations are being overcome through the advancement of technology and computing resources. While this technology has not quite evolved to be feasible for each and every application, there are emerging applications that could currently benefit; some examples in which this technology could readily impact industrial and security non-destructive testing include:

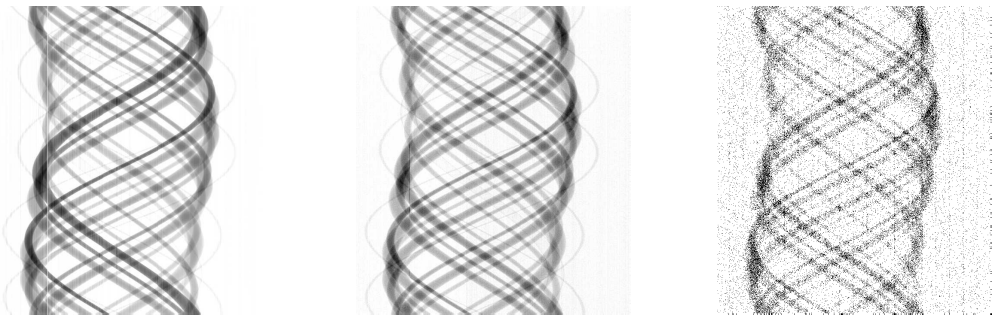

Figure 3.1: Sample sinogram data across various channels from the modified Multix ME100 linear array.

Materials Classification

As mentioned earlier, Jimenez et. al.[22, 27, 24] investigated radiography-based methods to identify materials based off of the x-ray transmission signature in numerical studies while Collins et. al.[7] investigated this experimentally. Although some k-edges could be resolved both numerically and experimentally, the data was generally too noisy. Separately, Wurtz et. al. [39] proposed a method to perform some limited materials classification which Jimenez et. al.[20] showed potential in combining this method with energy-resolved information to expand the capability of the Wurtz et. al. approach.

The expectation is that with multi-channel radiography data, the signal has a more direct correlation with the energy dependent attenuation profile compared to traditional imaging detectors; can one leverage this to distinguish between materials of similar composition? Additionally, will multi-perspective data from CT sufficiently suppress noise to reliably perform materials classification/identification tasks?

Data Quality

There are many motivating factors that lead the industrial non-destructive testing and evaluation community to pursue better quality data than what is currently available. Energy-resolved radiography could be one path to better data through rejection of information-starved channels and weighing of channels that contain high amounts of relevant information. However, as Roessl and Proksa[37] point out, using single or limited bins of information could lead to photon starvation thus effectively degrading signal-to-noise; although this could indeed be an issue in practice, for this work, industrial applications are only considered (as opposed to medical) and thus for almost all possible relevant absorbers, radiation dose is not a concern.

CT Reconstruction Quality

Building on the possible benefits mentioned above, computed tomography reconstruction would also benefit. Many popular reconstruction algorithms used in the non-destructive testing and evaluation community, such as the FDK algorithm by Feldkamp, Davis, and Kress[13], assume that a linear operator defines the imaging system; for traditional radiography this cannot be the case when using a Bremsstrahlung source, an absorber, and an integrating detector. For energy-resolved CT, using a single bin of information to generate sinogram data could potentially more closely approximate a linear system thus providing a more accurate reconstruction both numerically and spatially if noise does not dominate the data.

Two works that cause some concern in our investigation are those by Wang et. al. [38] and Ding et. al.[10] which show severe artifacts in reconstruction when using photon-counting data. Wang et. al. claim this is due to random variations in energy response while Ding et. al. claim the corruption comes from spectral distortions caused by the variation in the spectral absorption throughout the scan process. Both works provide reconstruction examples of cylindrical phantoms that indeed show essentially unusable reconstructions due to severe artifacts.

Approach

This work will evaluate data quality for CT performance with respect to three performance goals by acquiring a single slice Color CT dataset and reconstructing each individual channel separately. First, the reconstructed data will be used to evaluate the waveforms and their corresponding signal-to-noise with respect to channel from the reconstructed voxels for various materials, in particular materials of similar composition; second, artifact reduction will be evaluated compared to a traditional CT dataset; finally, a comparison of different reconstruction algorithms on the same input energy-resolved input sinogram to evaluate numerical differences.

Experimental Design

All sinogram data was acquired using the system and geometry in our laboratory described above in section 3 with a source-to-object distance of approximately 1.68m. All scans consisted of 720 projections at 250keV and 0.5mA with an exposure time of one second per projection. The majority of scans were performed were reconstructed using Recon, a reconstruction algorithm developed by Los Alamos National Laboratories and Sandia National Laboratories [23, 32]; for comparison, one dataset was also reconstructed with a third-party reconstruction algorithm. It should be noted that only a single point gain correction was

made to the data and no calibration was done to account for spectral drift/distortion as this work is currently under way and will be reported in future work. Four objects were scanned:

1. **Wide Spectrum Survey:** This scan consists of 17 cylindrical samples in a circular orientation consisting of an empty polyethylene bottle, Nylatron, Delrin, SAE 30 motor oil , acrylic, nylon, two samples of water, teflon, polyethylene, the soft-drink Pepsi, lexan, the diet soft-drink Diet Coke, aluminum, magnesium, salt, and phenolic. All granular materials and liquids are contained in the same type of bottle as the empty bottle listed. The solid materials are cylindrical in shape with a diameter of approximately 12mm and the bottled materials have a 25mm diameter with a 1.1m wall-thickness.

2. **Simulant:** Two 0.45 kilogram simulants that simulate two different but similar simulants were scanned within the same field-of-view to evaluate whether the reconstructed waveform signatures can be distinguished based on particular type of simulant.

3. **Sugar-based Soft Drinks:** Three different types of sugar-based soft drinks in aluminum cans were scanned within the same field-of-view to evaluate whether the waveform signatures from the reconstructed voxels will allow one to distinguish between similar types of sugar-based soft drinks. This dataset was reconstructed using Recon as well as a popular third-party reconstruction algorithm to evaluate statistical numerical behavior.

4. **Wax and Wax-Aluminum Powder Cylinders:** Two 7.5cm cylinders were scanned in the same field-of-view. The first cylinder consists of wax in a polyethylene bottle and the second consists of a mixutre of the same wax combined with aluminum powder. This scan was done to evaluate beam-hardening artifacts between energy-resolved CT and traditional CT. In order to preserve resolution, a surrogate for the traditional CT dataset was used which consisted of the summation of all channels to produce single sinogram which was then reconstructed using the same reconstruction algorithm.

Results

Wide Spectrum Survey

Figure 3.2 shows a single bin reconstruction of the wide spectrum scan. It should be noted that the 4 circular regions at approximately the north-east-south-west positions are aluminum rods that hold the fixutre together and are not included in the evaluation. Figures 3.3 and 3.4 show the average waveform of the two soft drinks and water samples along with signal-to-noise ratios respectively; which seems to imply that the main absorber in this subset is the sugar contained within the Pepsi as Diet Coke is visually indistinguishable to the two samples of water, the signal-to-noise ratios of these regions do not indicate a degraded signal for any of the materials. It should be noted that all figures reconstructed using Recon

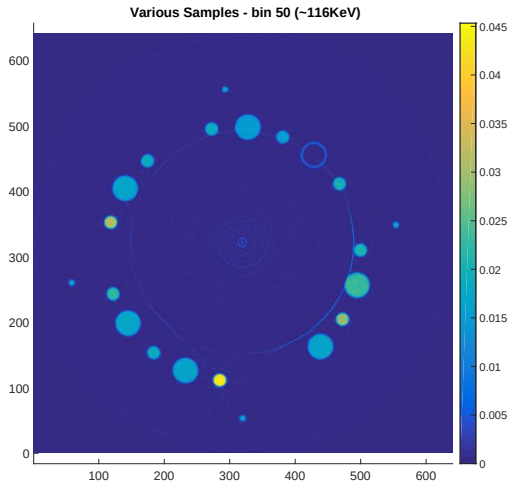

Figure 3.2: Single bin reconstruction of various plastics, liquids, and metals (bin 50, 116keV).

contain error bars from the sample of voxels evaluated which indicate that there was very little relative variation in the waveforms for a given material.

Figures 3.5 and 3.6 compare the average waveforms of the air contained within the empty bottle and the air in the center of the reconstructed slice; while at first glance the waveforms seem to differ significantly, it should be noted that the signal-to-noise ratio was very low which would seem to indicate that insufficient absorption due to air and/or numerical processing in the reconstruction do not allow for a sufficient measurement.

Figures 3.7, 3.8, and 3.9 display the remaining waveforms which seem to indicate that each of the materials in the field-of-view can be distinguished visually based on the waveform.

Simulants

Figures 3.10 and 3.11 show a single-bin reconstruction of the simulants along with their average profiles respectively. It should be noted that the differences in intensity in figure 3.10 are essentially indistinguishable visually; however, when observing the full waveform, it is clear there is a significant difference between similar types of simulants.

Sugar-based Soft Drinks- Reconstruction Comparison

It is clear from figures 3.12 and 3.13 that there is a significant scaling and visual difference between the two reconstruction algorithms and both do not allow for visual differences

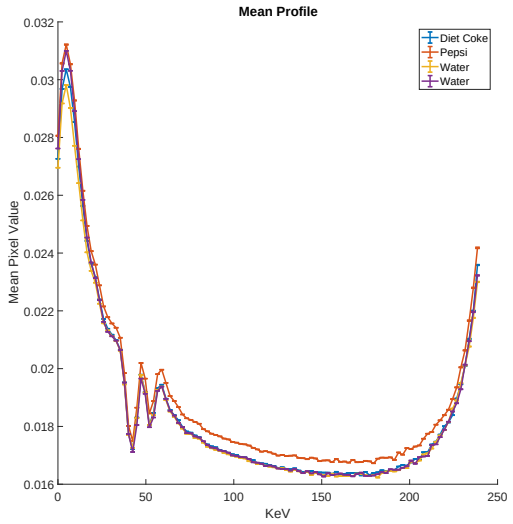

Figure 3.3: Average profile for Diet Coke, Pepsi, and Water from figure 3.2.

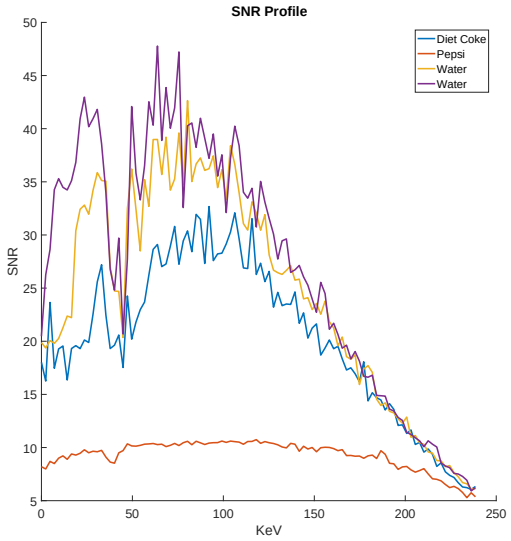

Figure 3.4: Signal-to-Noise profile for Diet Coke, Pepsi, and Water from figure 3.2.

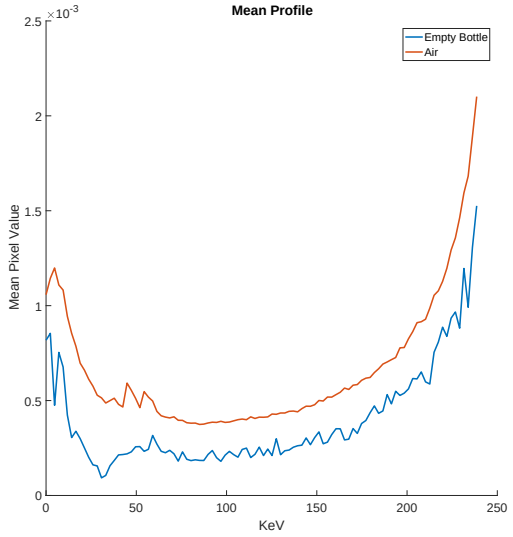

Figure 3.5: Average profile for Empty Bottle and Air from figure 3.2.

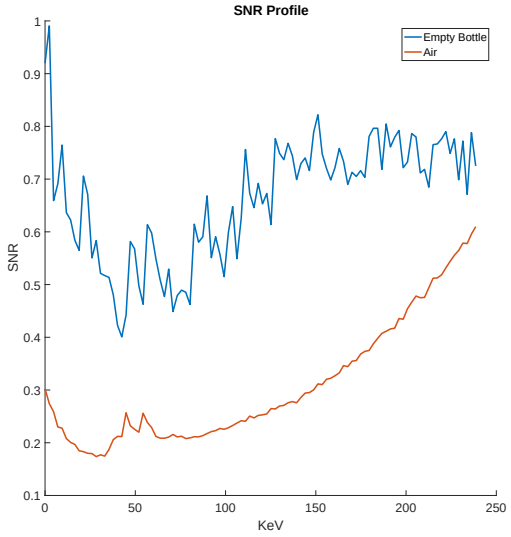

Figure 3.6: Signal-to-Noise profile for Empty Bottle and Air from figure 3.2.

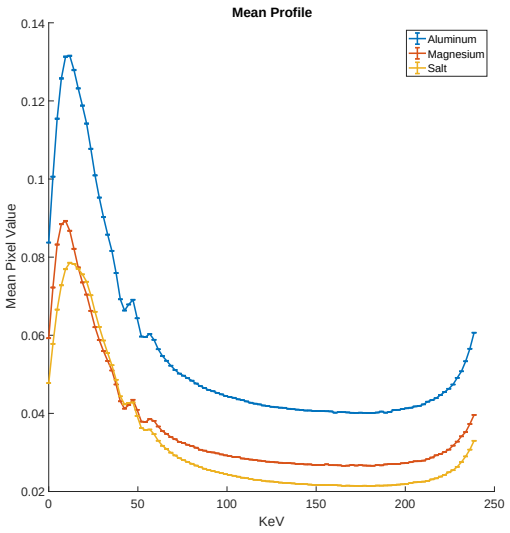

Figure 3.7: Average profile for Aluminium, Magnesium, and Salt from figure 3.2.

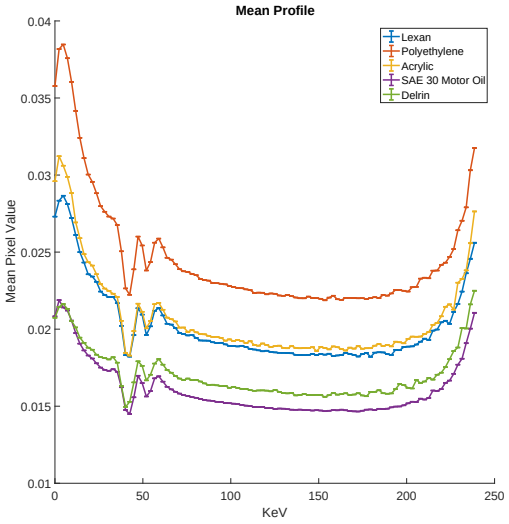

Figure 3.8: Average profile for Lexan, Polyethylene, Acrylic, SAE 30 Motor Oil, and Delrin from figure 3.2.

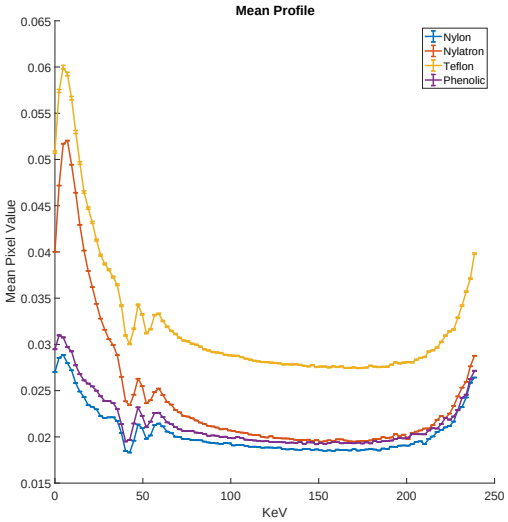

Figure 3.9: Average profile for Nylon, Nylatron, Teflon, and Phenolic from figure 3.2.

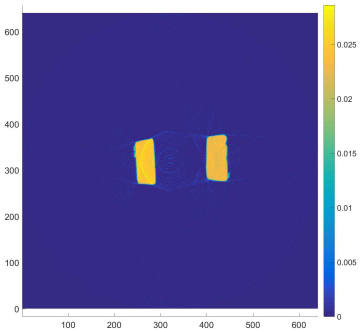

Figure 3.10: Single bin reconstruction of two similar simulants (bin 50, 116keV).

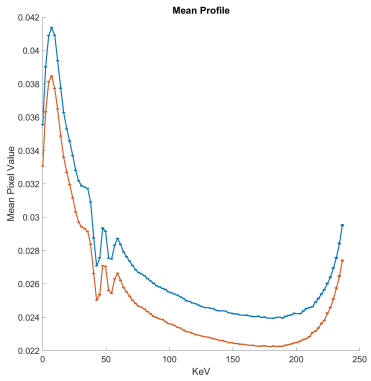

Figure 3.11: Average profile for two simulants from figure 3.10.

between different sugar-based soft drinks as shown in the waveforms of figures 3.14 and 3.15. It should be noted however that figure 3.16 seems to show large relative variability compared to Recon in voxel values within the same material; the source of this is not known as it is not clear what type of filters, scaling, or other processing is done by the third-party algorithm.

Artifact Reduction

Figures 3.17 and 3.18 show the reconstructed image of a single bin and of all bins summed respectively; it is clear that there are significant beam-hardening artifacts in the region between the two cylinders in the integrated signal reconstruction. Moreover, figure 3.19 shows further significant beam-hardening artifacts are seen within each cylinder for the integrated reconstruction compared to the single-bin reconstruction. As the circular regions have some noise to them, it is difficult to assess whether subtle beam-hardening artifacts are present in the single-bin reconstruction.

Conclusions

This work has demonstrated the emerging high-energy Color CT capability developed at Sandia National Laboratories. Initial results seem to hold much potential in the ability to non-destructively distinguish between similar materials and to achieve superior reconstruction by reducing reconstruction artifacts due to beam-hardening. The quality is only

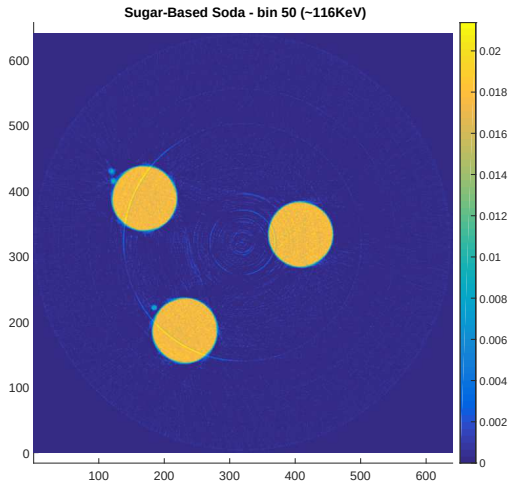

Figure 3.12: Reconstruction using Recon of three sugar-based soft drinks.

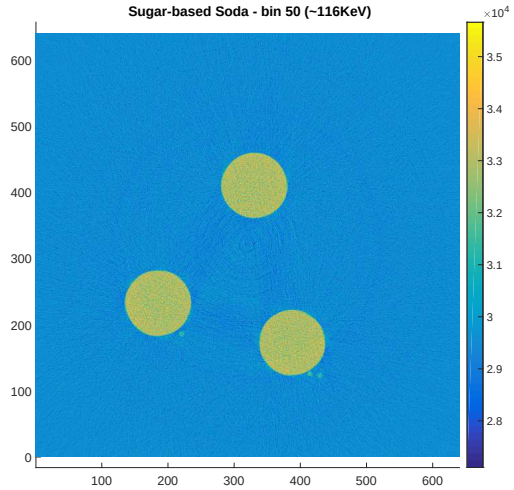

Figure 3.13: Reconstruction using 3rd-party reconstruction algorithm of 3 sugar-based soft drinks.

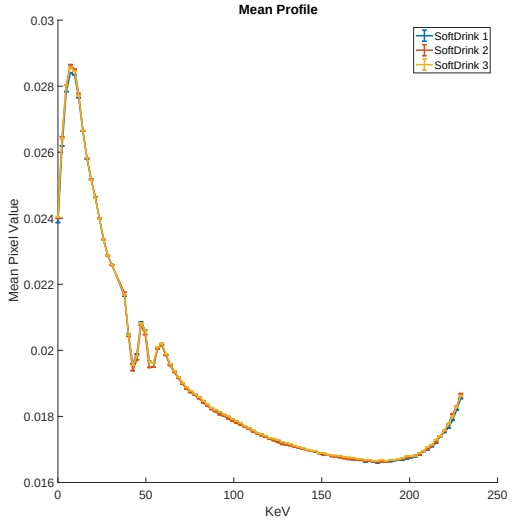

Figure 3.14: Average profile from Recon of sugar-based soft drinks.

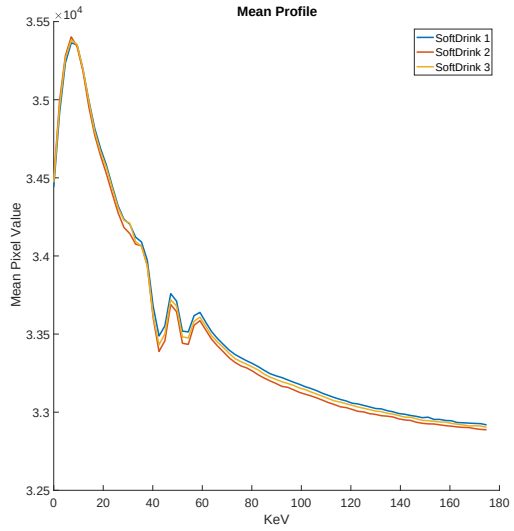

Figure 3.15: Average profile from 3rd-party reconstruction algorithm of 3 sugar-based soft drinks.

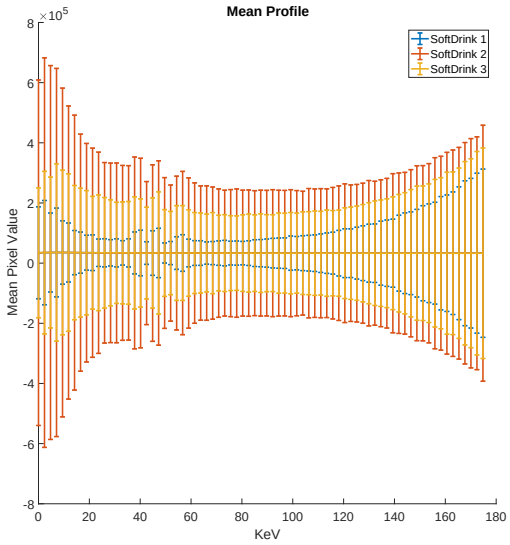

Figure 3.16: Average profile (with error bars) from 3rd-party reconstruction algorithm of 3 sugar-based soft drinks.

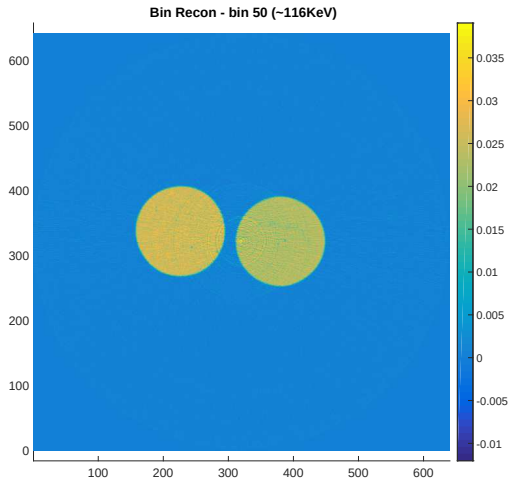

Figure 3.17: Single bin reconstruction.

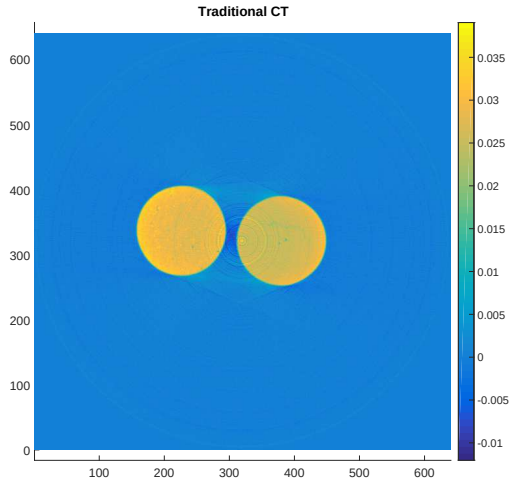

Figure 3.18: Integrated signal across all channels reconstructed.

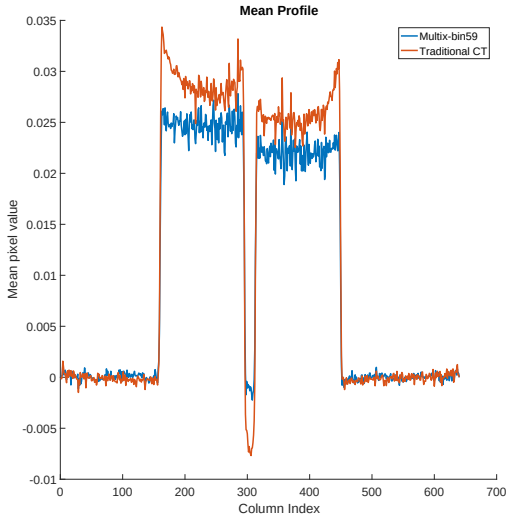

Figure 3.19: Line profile for figures 3.17 and 3.18.

expected to improve once a spectral correction process to applied to the data prior to reconstruction. Curiously, none of the degradations observed by Ding et. al. and Wang et. al. were observed, but will continue forward cautiously. Future work consists of not only developing a spectral correction process but also evaluating more complex objects and evaluating reconstruction data quality for suitability in segmentation and recognition applications. This technology has the potential to disrupt the Non-destructive testing and evaluation capability in numerous ways including counterfeit detection, quality assessment, materials identification, as well as verification and validation applications all of which are of significance to various areas within industry and security.

Chapter 4

Machine Learning for Industrial Material Classification Applications with Color CT Datasets

Summary

Sandia National Laboratories (SNL) has recently acquired a Multix multi-channel linear array detector calibrated for obtaining sinogram data up to 300 keV across 128 channels per pixel. This works aims to examine the utility of this color CT system for materials classification and identification purposes, with a focus on materials critical to industrial and security applications; namely, oils, water, plastics, copper, lead, and aluminum. Machine learning algorithms such as support vector machines and logistic regression will be investigated for distinguishing different materials of interest with similar absorption properties. Methods to properly adapt the aforementioned schemes for multichannel datasets, as well as possible reasons for an algorithm's lessened ability to label materials, will be highlighted. In addition, ensemble schemes like boosting will be explored to improve the robustness of the classification tasks. Collectively, this work aims to determine the optimal strategy for industrial material identification in the context of color CT datasets. The integration of machine learning towards this goal could have tremendous impact on the non-destructive evaluation community.

Introduction and Background

Computed tomography (CT) is a powerful modality for non-invasively detecting and identifying the contents of an object1. In conventional CT acquisition methods using Bremsstrahlung radiation sources, however, materials with different elemental compositions may appear alike. These difficulties arise because attenuation coefficients are not only determined by material composition, but also by the energies of the interacting photons. For certain energies, it is possible for two objects with varying atomic numbers to exhibit comparable attenuation coefficients. Such challenges for material classification are exacerbated in the presence of reconstruction and streaking artifacts due to beam hardening and insuf-

ficient penetration power, respectively[7]. Dual-energy schemes are a potential method to mitigate these undesirable effects, but often incur the cost of extended acquisition times and computationally demanding post-processing for large datasets.

While two dissimilar objects may not be distinguished from one another within a particular band of energies, they can be precisely separated using their fully characterized attenuation profiles as a function of energy. In this regard, spectral CT imaging serves as the optimal option for material classification purposes. Here, detectors not only count the number of incident photons, but also can resolve photon energy, leading to significantly more information being extracted for a given pixel from a computed tomography reconstruction. Stated differently, in a single acquisition protocol, complete attenuation curves for all imaged objects can be determined[22, 27, 24].

Considering this advantage, Sandia National Laboratories has recently acquired a color CT equipment consisting of five customized Multix ME100 modules calibrated for 300 keV across 128 channels[28]. The modules are configured into a linear array for a total of 640 pixels across a 0.5m field-of-view with four axis motion control (one rotary, three translation). The equipment includes a Comet x-ray source capable of up to 450keV/20uA, and has a source-to-detector distance of approximately 2.06m and an adjustable source-to-object distance. In this work, our objective is to evaluate the effectiveness of this system in classifying various objects (discussed in further detail below). As with many other energy-resolved applications, we are cognizant that noise from factors such as pulse pile-up, scatter, and spectral drift could confound our ability to perform this discrimination task. Interestingly, however, we have demonstrated in recent work that even materials with similar compositions can qualitatively be separated from one another using the energy-dependent attenuation waveforms derived from this system.

Given our prior findings, in this study, we focus on integrating the color CT data into advanced machine learning (ML) algorithms for automated material classification. More specifically, we investigate multiple supervised learning techniques to quantitatively and autonomously delineate different objects in the same field-of-view. ML has greatly benefited the scientific community by providing insight into correlations that otherwise could go unnoticed. Thus, the combination of multi-channel radiography data with ML could have tremendous impact on non-destructive evaluation for object detection purposes.

Dataset and Features

Using the Multix system described above (with a source-to-object distance of approximately 1.68m), two scans are performed. Both consisted of 720 projections at 250keV and 0.5mA with an exposure time of one second per projection. Reconstruction was performed with Recon, an algorithm developed by Los Alamos National Laboratories and Sandia National

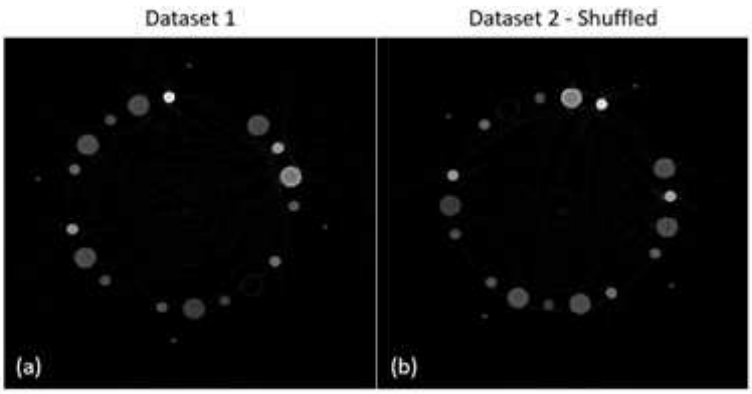

Figure 4.1: (a) Example image reconstructed from the 116 keV bin for dataset 1. (b) Corresponding image from dataset 2 with the same materials in a shuffled manner.

Laboratories. Note that only a single point gain correction was applied to the data. Furthermore, calibration to account for potential spectral drift/distortion was not employed.

The first dataset acquired includes 17 cylindrical samples in a circular orientation consisting of an empty polyethylene bottle, Nylatron, Delrin, SAE 30 motor oil, acrylic, nylon, two samples of water, teflon, polyethylene, soft-drink Pepsi, lexan, diet soft-drink Coke, aluminum, magnesium, salt, and phenolic. The second scan comprises of the same objects, but in a shuffled, alternate circular orientation. Note that all granular materials and liquids are contained in the same types of bottles. The solid materials are cylindrical in shape with a diameter of approximately 12mm, while the bottled materials have a 25mm diameter with a 1.1m wall-thickness. We deliberately chose the objects to vary significantly in their similarity to one another. This was done to thoroughly assess the capability of the Multix system as well as the applied machine learning techniques for material classification. Figure 4.1(a) and 4.1(b) showcase reconstructed images drawn from one energy bin for the two datasets.

In this work, we are interested in leveraging the first dataset for training the different ML algorithms. The second dataset, which comprises of the same materials as the first dataset but in a shuffled fashion, is utilized for assessing the agreement of each ML technique in determining the identity of an object. The input features into each ML technique varies, as described in the methods section below. In general, however, the features are either the attenuation profile (over the range of 0 keV to 250 keV) for each pixel spanning a particular object or the mean attenuation profile across all pixels for that object. Prior to training as well as validation, the attenuation profiles associated with each object in both datasets is normalized by rescaling the distribution of attenuation measurements across energy bins such that the mean of observed values is 0 and standard deviation is 1. This ensures scaling differences between the two datasets (i.e. due to differing gain settings, varying electronic

noise characteristics etc.) do not confound analyses.

Methods

With the exception of cosine similarity, all other algorithms are trained using error-correcting output codes (ECOC)[9]. This is a technique to extend classifiers typically used for binary applications to multiclass learning paradigms. In our case, because we are interested in distinguishing 17 materials, we train 136 binary classifiers (17(17-1)/2), each specialized in separating a unique pair of objects (i.e. aluminum vs. magnesium). The final output is determined with a majority voting scheme among the 136 classifiers. We explore three choices for the binary classifier, as discussed below.

Cosine Similarity

Cosine Similarity (CS) is a simple measure of similarity between a reference attenuation curve $x^{(ref)}$ and target attenuation curve $x^{(i)}$:

$$CS(x^{(i)}, x^{(ref)}) = \frac{x^{(ref)} * x^{(i)}}{\|x^{(ref)}\|_2 \|x^{(i)}\|_2}.$$

The smaller the CS metric, the greater the correlation between two profiles. Note that this metric is independent of scaling differences, and predominantly considers the shape of the attenuation profile. For each material in dataset 1, we designate $x^{(ref)}$ as the mean attenuation profile across all pixels spanning that material. The set of $x^{(i)}$ is the mean attenuation profiles for each material in dataset 2. Each object in dataset 2 is thus classified by find the $x^{(ref)}$ that minimizes CS. As mentioned, CS does not employ the ECOC method described above, however, the three techniques described immediately below do leverage it.

Logistic Regression

In Logistic Regression (LR), we model the output variables $y^{(i)}$, given the input features $x^{(i)}$ and model parameters (Θ), as a binomial distribution:

$$p(y^{(i)}|x^{(i)};\Theta) = (h_\Theta(x^{(i)})^{y^{(i)}})(1 - h_\Theta(x^{(i)}))^{1-y^{(i)}},$$

where $h_\Theta(x^{(i)})$ is defined as the sigmoid function. We assume the training samples are generated independently, and attempt to determine the Θ that maximize the joint likelihood:

$$\prod_{i=1}^{m} (h_\Theta(x^{(i)})^{y^{(i)}})(1 - h_\Theta(x^{(i)}))^{1-y^{(i)}}.$$

To make this problem more tractable, we instead maximize the log likelihood, which does not alter the end result:

$$\sum_{i=1}^{m} y^{(i)} \log(h_\Theta(x^{(i)})) + (1 - y^{(i)}) \log(1 - h_\Theta(x^{(i)})).$$

There is no closed form solution to this maximization problem, so we apply stochastic gradient ascent to iteratively determine the optimal Θ. Once the model parameters have been identified, to make a new prediction, we simply identify the label that maximizes $p(y^{(i)}|x^{(i)}; \Theta)$. In the context of our application, the set of $x^{(i)}$ represents attenuation profiles drawn from each pixel spanning the two objects under consideration.

Support Vector Machine

Support Vector Machines (SVMs) classify data by finding the optimal hyperplane that separates the two classes of interest. If the hyperplane is parameterized by (w, b), then to maximize the margin γ (i.e. the separation of the hyperplane and the training data), we solve the following optimization problem:

$$\underset{\hat{\gamma}, w, b}{min} \frac{\hat{\gamma}}{\|w\|_2} \text{ s.t. } \|w\|_2 = 1;\ y^{(i)}(w^T x^{(i)} + b) \geq \hat{\gamma},\ i = 1, ..., m.$$

This problem is difficult to solve, as the second constraint is non-convex. By way of a few simplifications, the optimization task can be reformulated as the following equivalent convex problem:

$$\underset{\hat{\gamma}, w, b}{min} \frac{1}{2}\|w\|_2^2 \text{ s.t. } y^{(i)}(w^T x^{(i)} + b) \geq 1,\ i = 1, ..., m.$$

This algorithm inherently assumes the dataset is linearly separable. For cases where this might not be true, we introduce slack variables (ξ) and $\boldsymbol{l}_2$ regularization, yielding another convex problem:

$$\underset{\hat{\gamma}, w, b}{min} \frac{1}{2}\|w\|_2^2 + c\sum_{i=1}^{m} \xi_i \text{ s.t. } y^{(i)}(w^T x^{(i)} + b) \geq 1 - \xi_i,\ i = 1, ..., m;\ \xi_i \geq 0.$$

The parameter c governs the extent to which training examples can have functional margins less than 1. As with LR, the set of $x^{(i)}$ to train each binary SVM classifier is the attenuation curves extracted from all pixels on the two materials.

Kernelized SVM

The dual of the above convex problem can be shown to operate on the input features only via inner products. We leverage this to apply the radial basis function kernel operator

with free parameter σ to our training samples:

$$k(x^{(i)}, x^{(j)}) = \exp\left(-\frac{\left\|x^{(i)} - x^{(j)}\right\|_2^2}{2\sigma^2}\right).$$

Kernels map the input training dataset to a higher dimensional space, where the classification task may be more tractable. The training features used for kernelized SVM are identical to those used for the standard SVM above.

Experiments

We evaluated the performance of different ML algorithms with two experiments. In the first, we divided the attenuation profiles derived from dataset 1 such that 70% are applied for training, and the remaining 30% are set aside for validation. Thus, in this case, both the training and testing happens within a single dataset (henceforth referred to as intra-dataset assessment). Note that this first experiment is not applicable to the CS algorithm, since training for this technique is based on the mean, as opposed to the pixel-by-pixel, attenuation profile for an object. In the second experiment, all the attenuation curves from dataset 1 are leveraged for training each ML technique. These are then assessed using the average attenuation profile for each material in dataset 2. Because we do not have access to the ground-truth identity of the materials in dataset 2, the purpose of the second experiment is to investigate the degree of agreement among the various algorithms.

Results and Discussion

A summary of the results for the first experiment using LR, SVM, and KSVM is presented in Figure 4.2. Among the different models trained, it is immediately evident that LR underperforms the most since it provides an overall intra-dataset object identification accuracy of only 30%. For certain materials, like air and aluminum, LR achieves a perfect performance. But, in the case of Nylon and Acrylic, for example, it entirely fails to identify them with a near 0% accuracy. This directly suggests that the attenuation profiles are not linearly separable, and thus, LR struggles for the classification task at hand. The trends observed with SVMs are more promising, however. As described above, the SVMs we apply include slack constraints to obviate the linear separability assumption. The benefits of this are apparent since materials like salt, magnesium, aluminum, oil, and Teflon are easily resolved by the algorithm. The primary case where SVM underperforms is in distinguishing diet coke, water, and Pepsi. Besides varying concentrations of sugar, these materials are predominantly water, which may potentially explain the low accuracies of SVM. Nonetheless, across all materials, the classification accuracy stands high at 82%. The introduction of a radial basis function kernel in SVM appears to negligibly affect performance. More specifically, the overall accuracy improves incrementally to 83%. This indicates that mapping of features to a higher-dimensional space using radial basis functions does not facilitate

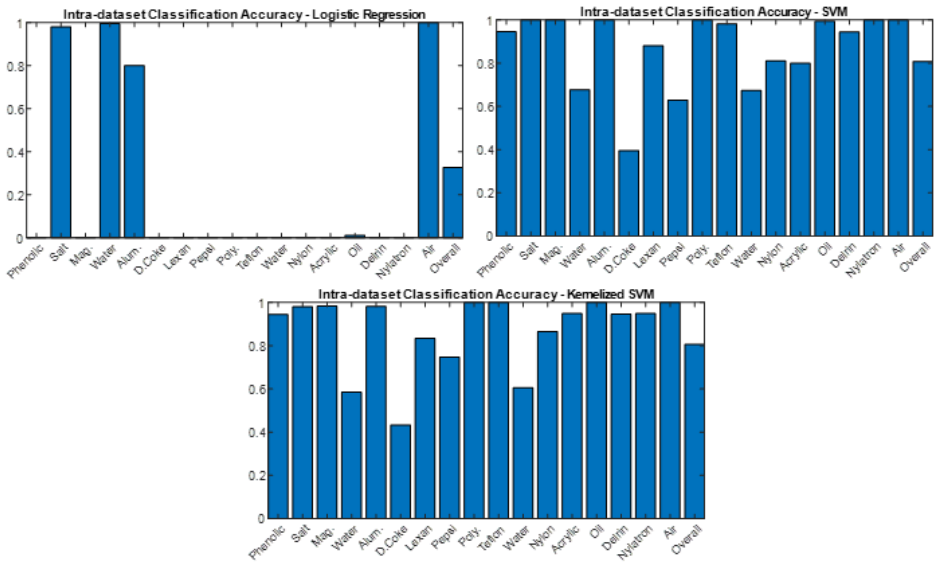

Figure 4.2: Intra-dataset classification accuracies for varying materials using different ML techniques. Logistic regression exhibits the lowest performance, while SVM with as well as without kernalization demonstrate accuracies that are superior and comparable to one another.

material detection. It is important to note, however, that linear and higher order polynomial kernels may be more useful.

Figure 4.3 highlights the outcomes of the second experiment, wherein the developed models are evaluated on the shuffled dataset. As in the results of the first experiment, LR performs poorly here as well. In particular, LR seems to favor designating the shuffled materials as either salt or water, which is clearly incorrect. This further supports the notion that models enforcing a linear decision boundary between different labels are not applicable for this task. Regarding CS and SVM, there is modest agreement between the outputs of these two techniques. Among the 17 different materials, CS and SVM agree on the identity in 8 cases. A closer look at the outcomes reveals that SVM might be a more robust approach. For example, based on visual inspection, it is apparent material 16 in dataset 2 represents the empty bottle. CS incorrectly labels material 16, however, as Delrin, whereas SVM properly marks it as air. SVM with kernelization provides the same results as SVM alone for all but two materials; namely, materials 9 and 13. The disagreement in the case of material 13 is whether the label is magnesium or aluminum. This uncertainly is reasonable given the similar atomic numbers of these two materials. Likewise, for material 9, while SVM predicts polyethylene, SVM with kernelization outputs acrylic. Interestingly, polyethylene

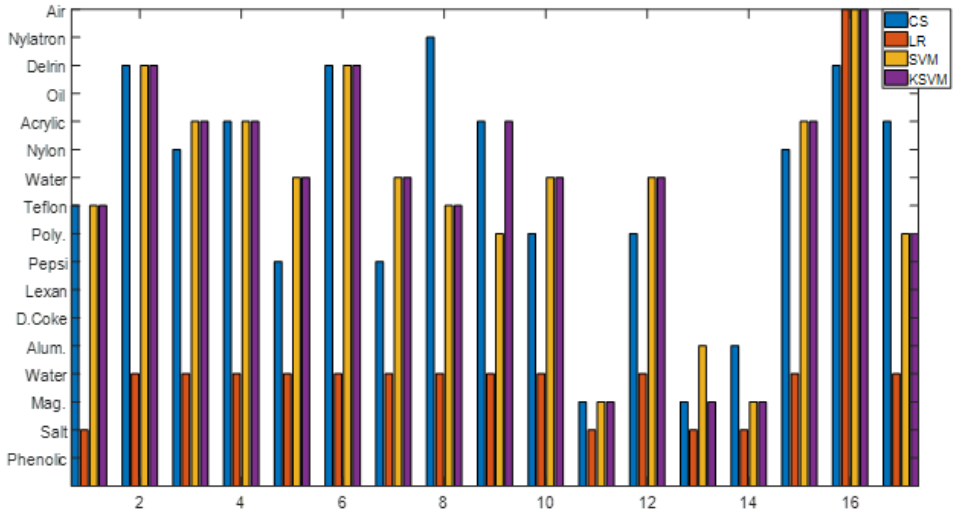

Figure 4.3: Classification outputs of CS, LR, SVM, and K-SVM when applied to dataset 2. Logistic regression entirely fails in this context to identify materials. CS and K-SVM, on the other hand, appear to properly distinguish materials from one another. It is interesting to note that CS and K-SVM also agree with one another in a majority of the cases.

and acrylic are plastics with similar composition, so the classifiers, at the very least, agree on the type of material. If a majority voting scheme among different classifiers is utilized (i.e. a boosting strategy), the final label will be acrylic, given that CS outputs this label as well. Overall, this analysis demonstrates that in cases where materials are erroneously labeled, the classifiers likely matched them to a substance with very similar composition. This capability is enabled by the complete attenuation profiles used in the training phase for different algorithms.

It is important to note that the trained classifiers do not designate any material as lexan or oil. We speculate that because lexan is a plastic, it is often misinterpreted as polystyrene or acrylic. The reason for oil being misclassified, however, is unclear. It might be that the type of oil used in dataset 2 varies from that in dataset 1. This will be examined more thoroughly in a later experiment.

Conclusion and Future Work

Collectively, this exploratory work presents a comparison of the effectiveness of different ML techniques to classify materials in multichannel, color CT datasets. We found several interesting trends in the results: (1) LR is not useful for the classification tasks at hand. This indicates that other linear classifiers (e.g. Nave Bayes) will also perform poorly, as the data is best segmented by a nonlinear decision boundary; (2) The SVM model (with slack variables) provides very high performance for intra-dataset classification. Qualitative analysis suggests good performance for classifying materials in a new dataset as well; (3) SVM with kernelization provides incremental benefits over SVM alone. This is a surprising result, especially given that it is good practice to kernelize features; (4) The CS metric, though simple, demonstrates the ability to match the outcomes of more complex models like SVM. This suggests that that CS and SVM should be integrated with one another for potentially more robust performance.

A major limitation of this study is the limited size of the training and testing sets. We are confident that collecting more data would pave the way for higher performance in discriminating different materials. In addition, we hope to acquire data with ground-truth labels, as this will facilitate the validation phase. In a future work, it is also our goal to employ more thorough metrics to evaluate difference ML techniques. The analysis of accuracy alone hides information such as false positive and false negative characteristics. This motivates the need for computing precision, recall, and f-score for each ML algorithm. Moving ahead, we are prioritizing the implementation of neural networks for the same classification tasks as in this study. Neural networks can capture more complex features in the datasets compared to traditional algorithms like SVM or LR. Thus, we aim to examine multilayer perceptrons as well as convolutional neural networks to distinguish materials with a higher accuracy.

Chapter 5

Unsupervised Learning Methods to Perform Material Identification Tasks on Spectral Computed Tomography Data

Summary

Sandia National Laboratories has developed a method which combines machine learning methods with high-energy spectral x-ray computed tomography data to identify materials' compositions within each reconstructed voxel in the field-of-view. While initial experiments led by Koundinyan, et al. [**?**] showed that machine learning methods such as support vector machines, neural networks, and deep learning perform well in identifying a variety of classes of materials such as oils, water-based liquids, plastics, and metals, this work seeks to identify material signatures using unsupervised clustering methods. Specifically, this work presents an unsupervised approach that can differentiate isolated materials with highly similar compositions. By applying this method to spectral computed tomography data, material identification can be performed more accurately than material identification performed on traditional single-channel computed tomography data. Additionally, if regions of the spectrum for several voxels become unusable due to artifacts, this method can still reliably identify a material. This capability has the potential to have tremendous impact in a variety of fields which leverage non-destructive evaluation for detection, verification, and validation applications in security, industry, and medicine.

Introduction

Computed tomography (CT) is a critical tool in the non-destructive analysis of objects and materials. While traditional CT methods using Bremsstrahlung radiation sources suffer from noise and artifacts due to lack of penetration or nonlinearities in material absorption (i.e. beam hardening), high-energy spectral CT can enhance performance by generating higher-quality images . This work uses the multichannel color CT system developed at Sandia

National Laboratories (SNL) by Jimenez et al. [20, 28], which produces energy-resolved data that correlate with materials' attenuation profiles. Spectral CT data also provide increased information for analysis than traditional CT data, indicating that multichannel CT data approaches possess higher potential to identify and analyze materials.

This work characterizes individual voxels in multichannel CT reconstructions. Previous work was done by Collins et al. [7] and Jimenez et al. [24] to investigate material identification using spectral CT by analyzing attenuation with the Lambert-Beer law, given by

$$I(\epsilon) = I_0(\epsilon)\, e^{-\mu(\epsilon)x} \tag{5.1}$$

where $I(\epsilon)$ is the photon count at energy ϵ, x is the source-to-detector distance traversed by the photon, and $\mu(\epsilon)$ is the attenuation coefficient. However, accurately determining $\mu(\epsilon)$ is often intractable in practice. Success of an unsupervised machine learning approach eliminates the need to analyze the Lambert-Beer law in material identification.

This work develops an iterative variation of hierarchical clustering, referred to as iterative hierarchical clustering, that can distinguish between materials with highly similar compositions. In this paper, first the high-energy spectral CT system is described in further detail. Second, the features of each dataset are discussed. Next, an iterative hierarchical clustering algorithm is presented, including the pre-processing of the data before applying the method. Finally, the algorithm performance is evaluated against other common unsupervised clustering methods.

Background

High-Energy Spectral X-Ray Computed Tomography

The high-energy spectral x-ray CT system developed by SNL and described in Jimenez et al. [28] consists of a Comet x-ray source and a detector composed of five customized Multix ME100 modules. The source has a maximum capability of 450 keV, which allows for improved penetration and reduced artifacts compared to traditional lower-energy sources. Additionally, the source has a high flux capability, which results in a high signal-to-noise ratio. The detector is an array of 640 pixels calibrated for 300 keV across 128 channels. The detector produces energy-resolved data, such that when a photon hits a pixel of the detector, the photon is binned into one of 128 channels based on its energy. The source-to-detector distance is approximately 2.05 meters.

In traditional systems, the energies of each photon cannot be determined or resolved. This means that each voxel in a reconstructed scan only has a single value associated with it, rather than a spectrum of values. Additionally, artifacts are more prevalent in traditional CT systems, particularly the beam hardening artifacts associated with high-density materials. The spectral data obtainable only with the spectral CT system provide important additional information needed for material identification.

Unsupervised Clustering Algorithms

Image segmentation plays a key role in the analysis of CT scans. Partitioning a scan into different components based on pixel characteristics provides valuable information for the identification and evaluation of different materials in the image. While Koundinyan et al. [30] investigated supervised approaches for the segmentation of high-energy multichannel CT scans, the work presented here investigates unsupervised approaches.

Three commonly-used distance-based unsupervised clustering algorithms include centroid-based, density-based, and connectivity-based algorithms. These algorithms find relationships between data points by analyzing the similarity or dissimilarity between pairs or collections of objects in a dataset; the similarity measure is defined as a distance metric, such as Euclidean distance, cosine distance, or Manhattan distance[16]. Euclidean distance is used as the distance metric in all algorithms in this work.

Each of these algorithms operates well only under certain conditions and constraints, often making the algorithms unsuitable for datasets that fail to meet these assumptions. For example, k-means clustering, a type of centroid-based clustering, requires that clusters are hyper-spherical or hyper-ellipsoidal[17]. A density-based approach known as DBSCAN, on the other hand, can find arbitrarily-shaped clusters[12], but requires that clusters have similar and uniform densities[11]. These constraints affect the performance of a clustering algorithm on a given dataset.

This work focuses on a variation of agglomerative hierarchical clustering, a type of connectivity-based clustering that forms a nested hierarchy of clusters. Traditional agglomerative hierarchical clustering begins by forming singleton clusters of each point in the dataset, and then merges nearby clusters until all clusters have been merged into a single cluster that contains all points in the dataset. The merging of clusters depends on the distance and linkage metrics, where the linkage metric determines how the distance between clusters is computed. Single-linkage, for example, finds the minimum distance between points in the clusters to determine their similarity, while complete-linkage finds the maximum distance between points in the clusters[3]. Single-linkage is used as the linkage metric in this work.

Approach

This work evaluates the performance of different unsupervised clustering algorithms on six datasets, described below:

1. **Shape Charge** (figure 5.1a)**:** Two materials are arranged concentrically to form an annular cylinder. This object is chosen because it is composed of multiple distinct materials arranged in a complex geometry; the annular shape, in particular, may increase beam hardening artifacts. Additionally, the contact between materials may cause obfuscation, making the material identification task more difficult.

2. **Ceramic Cylinders** (figure 5.1b)**:** Six ceramic cylinders of different materials are arranged in a circular orientation. In clockwise order beginning with the lower right cylinder, the cylinders are composed of room-temperature glass mica, high-temperature glass mica, alumina-silicate, alumina-bisque, alumina, and water-resistant zirconia. In contrast to the shape charge data, the ceramics are isolated, eliminating some of the beam-hardening artifacts. However, their compositions are more similar to each other than those in the shape charge data.

3. **Ceramic Cylinders with Steel Penny and Wood Block** (figure 5.1c)**:** A steel penny is added to the circular arrangement of ceramic cylinders, and a wood block is added to the center of this arrangement. The penny and block create additional beam-hardening artifacts because they absorb signal, thus making the ceramic cylinders more difficult to identify.

4. **Simulated Traditional CT Scan of Shape Charge:** A single-channel CT scan of the shape charge is simulated by summing the pixel values across all channels for each pixel in the scan. The simulated scan is used to compare the performance of different clustering algorithms on multichannel data with their performance on single-channel data.

5. **Simulated Traditional CT Scan of Ceramic Cylinders:** The ceramic cylinders CT dataset is reconstructed using the summation of the filtered sinogram data, which mimics traditional single-channel reconstruction. The expected behavior is that beam-hardening artifacts will be more prevalent, making the identification process more difficult. This is also to compare different algorithms on multichannel data and single-channel data.

6. **Simulated Traditional CT Scan of Ceramic Cylinders with Steel Penny and Wood Block:** The same process used to produce the simulated traditional CT scan of ceramic cylinders is applied to the ceramic cylinders with the addition of the penny and block.

(a) Shape charge. (b) Ceramic cylinders. (c) Ceramic cylinders with penny and wood.

Figure 5.1: Example scans from Channel 35.

The first three datasets were acquired using the system described in section 5. The shape charge dataset was collected at 400 keV and 2.3 mA with a source-to-object distance of approximately 0.64 meters. The ceramic cylinders datasets were collected at 250 keV and 0.5 mA with a source-to-object distance of approximately 1.75 meters. For each dataset, a single slice was selected and analyzed; therefore, rather than analyzing three-dimensional voxels, this work only analyzes two-dimensional pixels.

Two types of data are associated with each scan: spectral data and spatial data. The spectral data consist of the pixel values for a given pixel across all 128 channels, i.e. a 128-dimensional vector of pixel values; pixel value plotted against channel is the profile for a given pixel. The spatial data consist of two-dimensional vectors corresponding to the coordinate location of each pixel in the scan.

Features of Datasets

The materials in the shape charge are in contact with each other, which creates additional noise due to scatter and beam hardening. In particular, ring artifacts are prevalent in this scan. The spectral data are distinct for each material, as shown by their mean profiles in figure 5.2.

The materials in the ceramic cylinders datasets are isolated, which partially eliminates the noise and reconstruction artifacts present in the scan of the shape charge. However, artifacts are still prevalent at the edges of each material, with the most significant artifacts around the zirconia cylinder. Consequently, the spectral data for the pixels corresponding to the zirconia cylinder have the most variance. The spectral data are varied in distinguishability; specifically, alumina-silicate, glass mica, and high-temperature glass mica are highly similar in their spectral data, as shown in figure 5.3.

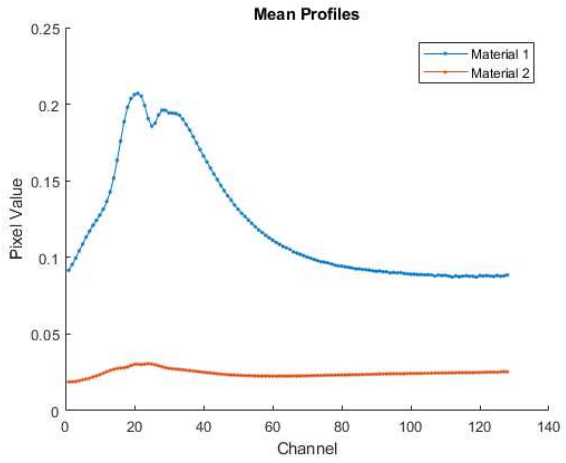

Figure 5.2: Mean profiles for shape charge data.

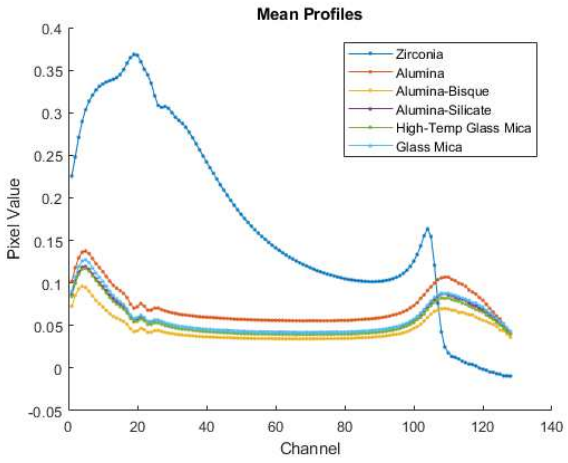

Figure 5.3: Mean profiles for ceramic cylinders data.

Implementation

Because this work focuses on identifying materials of highly similar compositions, this section focuses on the ceramic cylinders datasets. Iterative hierarchical clustering in relation to the shape charge and the simulated single-channel CT scans is discussed in further detail in section 5. The following processes are implemented in MATLAB.

Pre-Processing

Pre-processing the ceramic cylinders datasets consists of three steps: applying multilevel thresholding, eroding the binary image of the scan, and applying a box filter. This methodology identifies the pixels of interest for analysis and reduces the impact of noise and artifacts during the clustering task.

First, a single slice is chosen from the dataset. This slice has 128 images associated with it, i.e. one image for each channel. From this set, a single channel is chosen, identifying one greyscale image. This image serves as the initial input image. Multilevel thresholding using Otsu's method is applied to this input image, which partitions the pixels into a predefined number of classes based on pixel value [33, 1]. Because of differing pixel intensities, multilevel thresholding separates pixels corresponding to materials from pixels corresponding to air; only pixels corresponding to materials are saved.

As discussed in section 5, artifacts exist along the edges of the ceramic cylinders. Erosion of the image addresses this issue. After multilevel thresholding is performed, the remaining pixels are converted into a binary image. Using a flat disk-shaped structuring element, an erosion operation is performed on the binary image, removing the pixels around the edges of each isolated cylinder. This process is shown in figure 5.4.

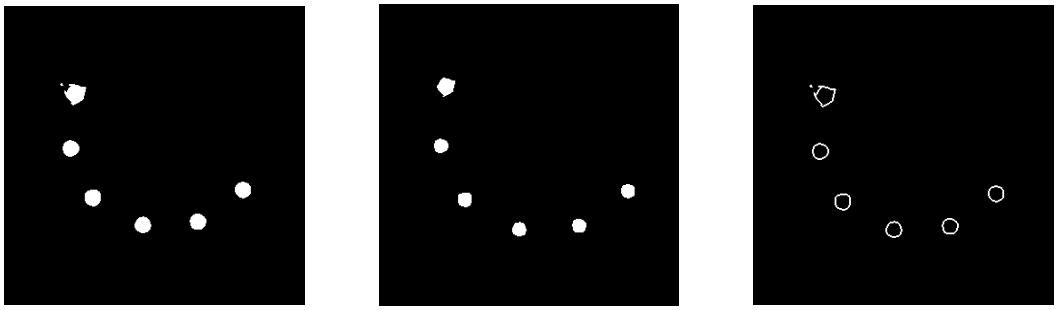

(a) Before erosion. (b) After erosion. (c) Removed pixels.

Figure 5.4: Binary images for erosion process.

Finally, after the pixels of interest have been selected, a 3×3 box filter is applied to smooth the scan. Because there are 128 images corresponding to a given slice, the box filter is applied to all 128 images.

An example of the effect of pre-processing on the pixel profiles is shown in figure 5.5. Pre-processing the scan reduces the variance of the spectral data for each material without significantly changing the mean profile, as shown in figures 5.6 and 5.7. Note that the zirconia cylinder has the most variability in its statistics because of the significant artifacts present on its edges.

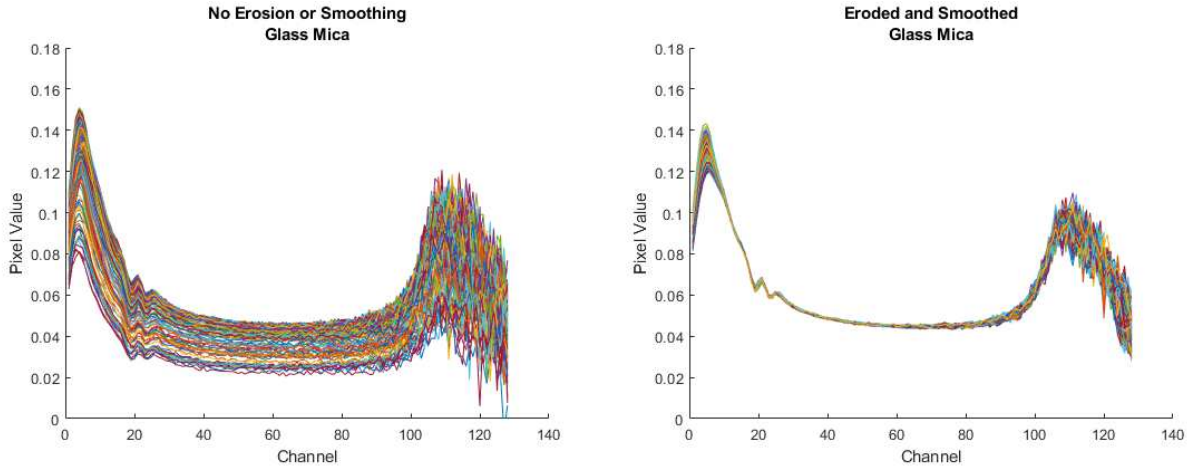

(a) Before pre-processing data.

(b) After pre-processing data.

Figure 5.5: Effect of erosion and smoothing on profiles for glass mica.

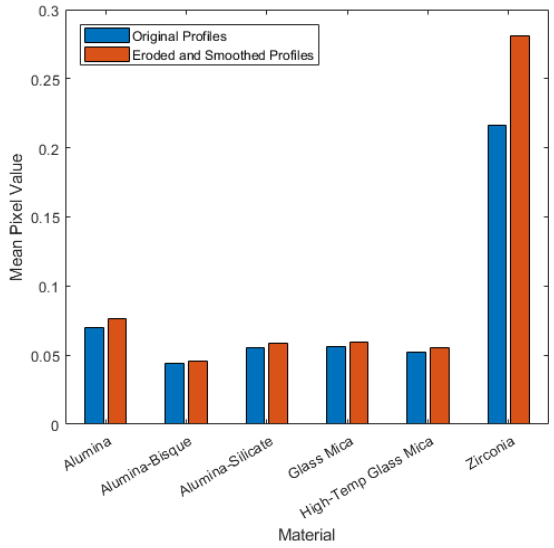

Figure 5.6: Mean profile values before and after pre-processing.

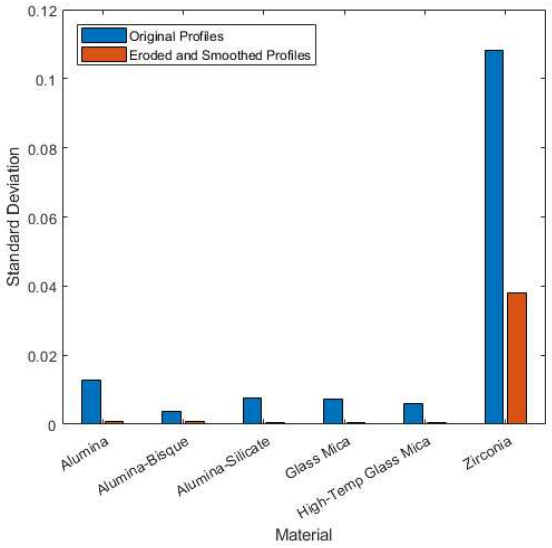

Figure 5.7: Standard deviation of mean values before and after pre-processing.

Iterative Hierarchical Clustering

Iterative hierarchical clustering is a variation of traditional hierarchical clustering, with one key modification: this algorithm uses hierarchical clustering iteratively as a binary classifier, rather than separating the data into multiple clusters in a single iteration. With each iteration, the dataset is reduced by removing points that have already been clustered. This means that clusters can have different densities; for example, once a cluster of low density is labeled and removed from the dataset, the algorithm performs only on higher-density clusters with reduced hindrance from highly variable cluster distributions.

The following algorithm describes the basic steps of iterative hierarchical clustering. The user must define the parameter `NUMCLUSTERS`, which specifies how many clusters the algorithm will identify. For the MATLAB implementation used in this work, single-linkage agglomerative hierarchical clustering is used.

1. Define parameter `NUMCLUSTERS`.
2. Calculate the connectivity matrix by finding the pairwise Euclidean distances between all elements of the spectral data, i.e. the pairwise distance between all profiles.
3. Perform hierarchical clustering to produce two clusters.
4. Form a cluster from the smaller of the two clusters. Record these pixels. The pixels belonging to the larger of the two clusters are considered unlabeled.
5. Remove the pixels in the smaller cluster from the dataset.
6. Repeat Steps 2-5 on the reduced dataset. Repeat `NUMCLUSTERS` - 1 times.
7. Only `NUMCLUSTERS` - 1 clusters are formed with Steps 1-6, and a subset of pixels will remain unlabeled. These remaining pixels are grouped together to form the final cluster.

All points are assigned to a cluster according to this algorithm, including potential outliers. Further analysis may be done on the points that remain unlabeled after Step 6 to identify outliers. Note that some initial analysis must also be done to identify the `NUMCLUSTERS` parameter.

Variations of Iterative Hierarchical Clustering

In the above algorithm, only spectral data are used to find similarity between data points. The incorporation of spatial data may help to differentiate pixels that may be spectrally similar but spatially distinct. Additionally, it incorporates the notion that pixels located near each other in a scan are more likely to be composed of the same material than pixels distant from each other. Furthermore, distance metrics for high-dimensional data

may inadequately represent the similarity between data points[34, 16], or, in other cases, high-dimensionality may add irrelevant information that hinders the clustering process[3]; adding the spatial similarity metric helps to address these issues. Other image segmentation algorithms have been presented that combine spectral data and spatial data, but these are applied to centroid-based clustering algorithms, which may be unsuitable for the ceramic cylinders datasets[6, 18].

There are multiple options for incorporating spatial data into the iterative hierarchical clustering process. One method is to calculate an additional connectivity matrix, where the elements of this second matrix are the pairwise Euclidean distance between all elements of the spatial data, which are treated as weights for the values in the spectral data connectivity matrix. As such, the values in the spatial connectivity matrix are rescaled to values between 0 and 1. To combine these matrices, the Hadamard product of the spectral data connectivity matrix with the spatial data connectivity matrix is taken. Hierarchical clustering is performed using the combined connectivity matrix. Another method is to augment each 128-dimensional spectral data vector with the two-dimensional spatial data vector corresponding to a pixel's coordinates. Note that the spatial vectors may need to be rescaled to the range of the minimum and maximum values in the spectral data if there is a large difference in scale.

In a different variation of iterative hierarchical clustering, another parameter `MINPOINTS` can be added if the clusters are uniform in size and if the number of points in a cluster can be accurately estimated. This parameter specifies the minimum number of points needed to form a cluster. To incorporate the `MINPOINTS` parameter, hierarchical clustering is performed to form `N` clusters, beginning with `N` $= 2$. Hierarchical clustering is repeated with increasing values of `N` until the number of pixels in the `N` - 1 smallest clusters is greater than or equal to `MINPOINTS`. The pixels in the `N` - 1 smallest clusters form a single cluster and are then removed from the dataset. This process is repeated `NUMCLUSTERS` times. Not all points will necessarily be labeled when using the `MINPOINTS` parameter. Additionally, note that `MINPOINTS` must be less than or equal to the size of the smallest cluster for this algorithm to perform accurately.

For the results presented in section 5, the unmodified version of iterative hierarchical clustering is used on the shape charge data, as the number of pixels corresponding to Material 1 (153 pixels) is significantly smaller than the number of pixels corresponding to Material 2 (1335 pixels). In contrast, the ceramic cylinders are all similarly sized, so the `MINPOINTS` parameter is used to improve the performance of the iterative hierarchical clustering algorithm. The results of spatial iterative hierarchical clustering are briefly mentioned for the ceramic cylinders but are not discussed in depth.

Application of Iterative Hierarchical Clustering

Multichannel CT data can potentially be used in the validation and verification of unknown objects, where a scan of unidentified materials can be compared to a scan of previously

identified materials. If iterative hierarchical clustering is performed on a dataset of materials with unknown identities, the mean profiles of the pixels in each assigned cluster can be calculated and compared to the mean profiles of known materials. Iterative hierarchical clustering, used in combination with the algorithm described below, has the potential to match unknown materials with known materials of the same composition. Two sets of data are needed for the identification of unknown materials: testing data (unknown materials) and training data (known materials). Two additional parameters are also needed for this algorithm: `X` and `N`, where `X` is a subset of channels (chosen to ignore noise in lowest and highest channels) and `N` is the degree of a polynomial.

1. Define parameter `NUMCLUSTERS`, and perform iterative hierarchical clustering on testing data.

2. Find the mean profiles of the clusters in the testing data, and find the mean profiles of each known material in the training data.

3. Define parameters `X` and `N`. Fit an `N` degree polynomial to the portion of each mean profile in the testing and training data specified by `X`.

4. Calculate the Euclidean distance between the polynomial coefficients corresponding to each mean profile in the testing data and the polynomial coefficients corresponding to each mean profile in the training data.

5. Identify the minimum distance between a cluster in the testing set and a material in the training set using the distances calculated in Step 4. Repeat until all clusters in the testing data have been matched with materials in the training data.

It is important to note that this method has only been tested on the ceramic cylinders datasets. It is also important to note that this method currently assumes that each material in the training set corresponds to only one cluster in the testing set.

Results

Shape Charge

The pre-processing described in section 5 for the ceramic cylinders data was also applied to the shape charge data. Because of the complex geometry of the shape charge, it is important to note that traditional binary image erosion was not possible on this dataset. Instead, to replicate the erosion process, the pixels on the outer border of the shape charge and the pixels on the edges between materials were identified using multilevel thresholding and removed from the scan.

In addition to iterative hierarchical clustering, traditional agglomerative hierarchical, k-means, and DBSCAN clustering were applied to the shape charge dataset. All of these algorithms performed with 100% accuracy, with a one-to-one relationship between materials and labels. This perfect accuracy likely occurred because the two materials in the shape charge are spectrally very distinct.

To quantitatively compare these results, the purity of each clustering was calculated. Purity is calculated as

$$\text{purity}\left(\Omega, \mathbb{C}\right) = \frac{1}{N}\sum_{i=1}^{k} \max_j \left(\omega_i \cap c_j\right) \tag{5.2}$$

where $\Omega = \{\omega_1, \omega_2, ..., \omega_K\}$ is the set of clusters, $\mathbb{C} = \{c_1, c_2, ..., c_J\}$ is the set of classes, and N is the number of data points. Note that the purity value will always be between 0 and 1. In this context, purity measures how many labels are assigned to a given material, such that if a material consists of points all belonging to the same cluster, the purity value will equal 1. The purity values for the tested clustering algorithms on the shape charge data are shown in the column labeled "Purity: Materials" in table 5.1. However, because effective clustering for this data also means that each label is assigned to only one material, purity was also calculated for each label, such that each label was treated as a class and each material was treated as a cluster. In this context, a purity value of 1 means that the points corresponding to a given label all belong to the same material. The results for the purity of each label are shown in the column labeled "Purity: Labels" in table 5.1.

Table 5.1: Purity values for tested clustering algorithms on shape charge data.

Clustering Algorithm	**Purity: Materials**	**Purity: Labels**
Hierarchical	1	1
k-Means	1	1
DBSCAN	1	1
Iterative Hierarchical	1	1

While the results are not presented in depth here, it is important to note that a spatial variation of iterative hierarchical clustering mentioned in Sec 5 was also tested on the shape charge dataset. The spectral data were augmented with the rescaled spatial data for each pixel, and iterative hierarchical clustering was performed on this augmented matrix. The algorithm performed with 100% accuracy.

Ceramic Cylinders

The same algorithms tested on the shape charge data were tested on the ceramic cylinders data for comparison. The results of agglomerative hierarchical clustering, k-means clustering,

DBSCAN and iterative hierarchical clustering are presented in table 5.2 using the purity calculations described in section 5. Note that additional variations of centroid-based clustering, including fuzzy c-means clustering, were tested, with similar results to k-means clustering. Algorithms other than iterative hierarchical clustering were unable to accurately distinguish each material; in fact, alumina-silicate, glass mica, and high-temperature glass mica were clustered together as a single material with all tested algorithms other than iterative hierarchical clustering. The poor performance of these algorithms was likely due to the factors discussed in section 5. Exploratory analysis of the dataset indicated that the conditions for these algorithms were not fully met because of the presence of arbitrarily-shaped clusters and clusters of different densities.

Iterative hierarchical clustering performed significantly better than any other algorithm tested in this work. Specifically, using parameters of `NUMCLUSTERS` $= 6$ and `MINPOINTS` $= 150$, each label corresponded to a single material and each material corresponded to a single label, indicating accuracy of the clusters. Note that 21 points were unlabeled after the completion of program.

Label assignments for each material are shown in figures 5.8, 5.9, 5.10, and 5.11. Note that not all points are necessarily assigned a label with the DBSCAN algorithm, or with the iterative hierarchical clustering algorithm with the incorporation of the `MINPOINTS` parameter.

Table 5.2: Purity values for tested clustering algorithms on ceramic cylinders data.

Clustering Algorithm	**Purity: Materials**	**Purity: Labels**
Hierarchical	0.9920	0.3851
k-Means	0.8784	0.6912
DBSCAN	0.9869	0.6788
Iterative Hierarchical	1	1

The spatial variation of iterative hierarchical clustering mentioned in Sec 5 and presented for the shape charge data in Sec 5 was also tested on the ceramic cylinders dataset. The algorithm performed with 100% accuracy. Because the `MINPOINTS` parameter was not used, every point in the dataset was assigned a label. It is important to note that iterative hierarchical clustering did not perform with 100% accuracy on this dataset without the `MINPOINTS` parameter or the incorporation of spatial data.

Single-Channel Computed Tomography

To make the multichannel CT data and the single-channel CT data as comparable as possible, the same pre-processing that was performed on the multichannel CT data was

performed on the single-channel CT data for both the shape charge dataset and the ceramic cylinders dataset. The performance of k-means clustering and iterative hierarchical clustering are discussed in this section.

For the shape charge data, both k-means clustering and iterative hierarchical clustering had the same results with the single-channel data as the multichannel data, with 100% accuracy. For the ceramic cylinders data, k-means clustering performed similarly as it did on the multichannel data, while iterative hierarchical clustering with parameters `NUMCLUSTERS` $= 6$ and `MINPOINTS` $= 150$ performed worse on the single-channel data than it did on the multichannel data. However, iterative hierarchical clustering still performed better than k-means clustering on the single-channel data. Table 5.3 summarizes the purity values for the single-channel shape charge and ceramic cylinders datasets. Figures 5.12 and 5.13 show the label assignments of k-means clustering and iterative hierarchical clustering, respectively, for the single-channel ceramic cylinders dataset.

Table 5.3: Purity values for simulated single-channel CT data.

	Shape Charge Data		Ceramic Cylinders Data	
Clustering Algorithm	**Purity: Materials**	**Purity: Labels**	**Purity: Materials**	**Purity: Lab**
k-Means	1	1	0.8698	0.6879
Iterative Hierarchical	1	1	0.8734	0.8734

Identification of Unknown Materials

The method described in section 5 was testing using the six ceramic cylinders as the training data and the ceramic cylinders with the addition of the steel penny and wood block as the testing data. Both datasets were pre-processed using the methodology described in section 5. Iterative hierarchical clustering was performed using the parameter `NUMCLUSTERS` $= 7$. Note that, because the number of pixels belonging to the steel penny (61 pixels) is smaller than the number of pixels belonging to each ceramic cylinder (average 185 pixels), the `MINPOINTS` parameter was not used. The mean profile matching algorithm was performed with parameters `X` $= [10, 80]$ and `N` $= 4$. Under these parameters, pixels in the testing set were matched to their corresponding materials in the training set with 100% accuracy, as shown in figure 5.14. The process of identifying the mean profiles of the testing set is illustrated in figure 5.15.

This material inference process was also applied to the single-channel ceramic cylinders datasets. Because iterative hierarchical clustering performed very poorly on the single-channel ceramic cylinders data with the addition of the steel penny and wood block after initial pre-processing, additional erosion was done on the dataset to improve the clustering process. Additionally, because only a single value is associated with each pixel rather than

an entire profile, the polynomial fitting process could not be applied to the single-channel data. Instead, the mean values for the pixels in each cluster and in each material were compared to determine which cluster corresponded to which material. Only alumina-bisque and zirconia were correctly identified before the additional erosion, but after the additional erosion, alumina, alumina-bisque, glass mica, high-temperature glass mica, and zirconia were all correctly identified. However, alumina-silicate was incorrectly identified as glass mica and the steel penny was incorrectly identified as alumina. These results are shown in figure 5.16. This demonstrate that the iterative hierarchical method is promising for material inference given a testing and training set, but indicates that the multichannel spectral data may be necessary to perform this task with very high accuracy.

Identification of Materials in Raw Scan

In practice, the testing data for material inference may be a unprocessed scan, rather than a pre-processed scan such as the one used in profile-matching process described in sections 5 and 5. In this scenario, the profiles for every pixel in a reconstructed scan, rather than only the profiles of the pixels identified in the pre-processing methodology, are compared to the mean profiles of known materials in the training data. To perform this comparison, every profile in the testing data and every mean profile in the training data is fitted with an `N` degree polynomial, and the distances between polynomial coefficients were computed. Every pixel is labeled with the material in the training data corresponding to the shortest distance between polynomial coefficients. For each set of profiles in the testing data corresponding to a mean profile in the training data, only profiles within a certain standard deviation of the mean profile are kept, and profiles outside of this threshold are categorized as unlabeled. These unlabeled pixels are then analyzed to determine if they correspond to new materials in the testing data that were not present in the training data. Assuming that a 128-dimensional zero vector represents a pixel corresponding to air, the distances between unlabeled profiles and this zero vector are calculated; profiles outside a certain standard deviation of the mean distance are categorized as new materials.

This process was performed using a raw scan of the ceramic cylinders with the addition of the steel penny and wood block as the testing data, and a pre-processed scan of the ceramic cylinders as the training data. Using parameters $\texttt{X} = [10, 80]$ and $\texttt{N} = 4$ and using a threshold of two standard deviations from the mean, only alumina-bisque was correctly identified with 100% accuracy. Initial analysis shows that artifacts on the edges of the cylinders contributed to inaccuracies in the performance of the material inference process. A visualization of the ceramic cylinders in the training data is shown in figure 5.17a, alongisde the identified materials in the testing data in figure 5.17b and the ground truth for the testing data in figure 5.17c. The accuracy of the material inference process is quantified in figure 5.18. Note that the unlabeled pixels corresponding to the zirconia cylinder were classified as a new material.

Conclusion

This work has demonstrated the potential of iterative hierarchical clustering to differentiate materials of highly similar compositions using multichannel CT data. These initial results seem to indicate that, with current unsupervised clustering methods, the spectral data from the high-energy spectral CT system provide important additional information that makes material identification more effective than single-channel data from traditional CT systems, provided that proper pre-processing is applied to the data prior to analysis. The use of iterative hierarchical clustering also seems to have the potential to identify the compositions of unknown materials when used in combination with a dataset of known materials. These capabilities have the potential to improve assessment, identification, detection, and evaluation of objects and materials.

Future Work

Iterative hierarchical clustering assumes initial knowledge about the data set. For example, for accurate results, the number of materials in the object and, in some cases, the number of pixels corresponding to each material must be generally known. More work must be done to determine how to choose the `NUMCLUSTERS` and `MINPOINTS` parameters for datasets that have unknown characteristics. The generalizability and scalability of this algorithm must also be further investigated, particularly for larger datasets, datasets of materials of similar compositions that are not isolated, and datasets with more significant noise and artifacts. The distance metric and linkage metric should also be evaluated to determine how different choices of these parameters impact the performance of iterative hierarchical clustering. The algorithm that identifies unknown materials using a training dataset must also be tested for its generalizability to other datasets with more variable characteristics.

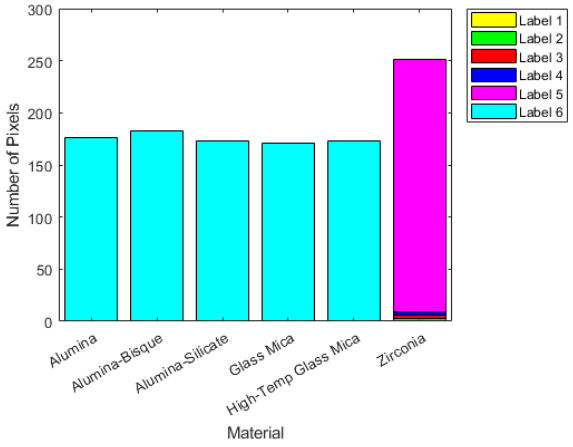

Figure 5.8: Label assignment for each material for agglomerative hierarchical clustering.

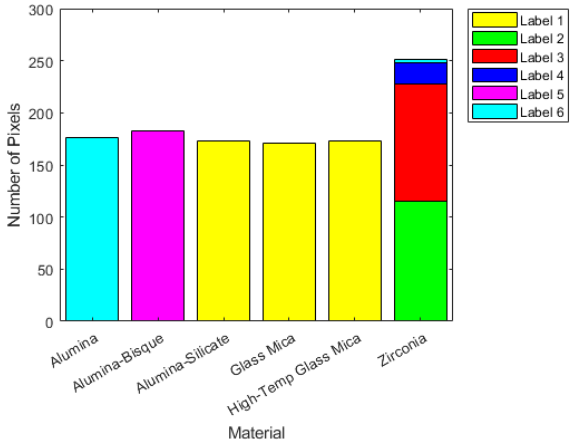

Figure 5.9: Label assignment for each material for k-means clustering.

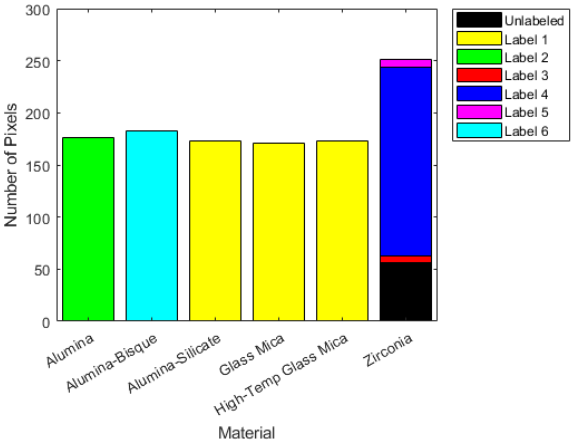

Figure 5.10: Label assignment for each material for DBSCAN.

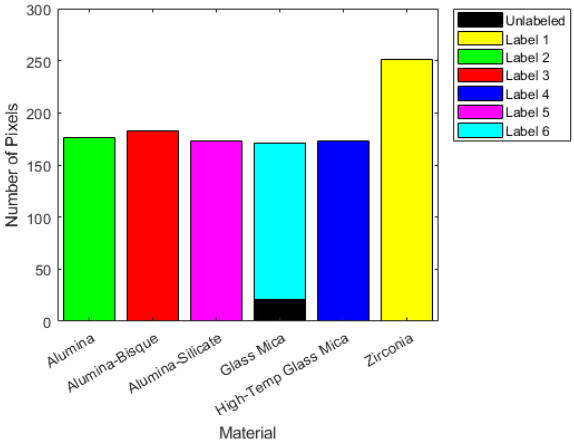

Figure 5.11: Label assignment for each material for iterative hierarchical clustering.

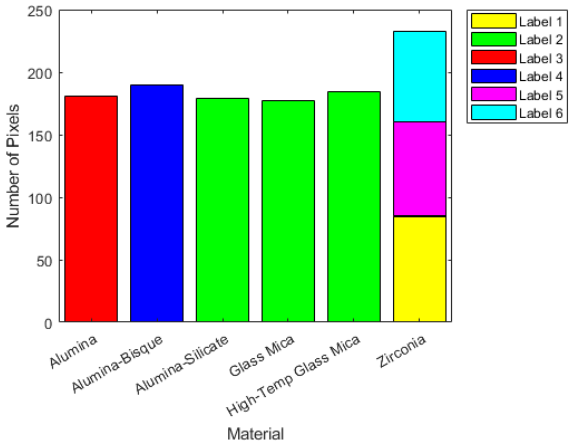

Figure 5.12: Label assignment for each material for k-means clustering on the single-channel ceramic cylinders data.

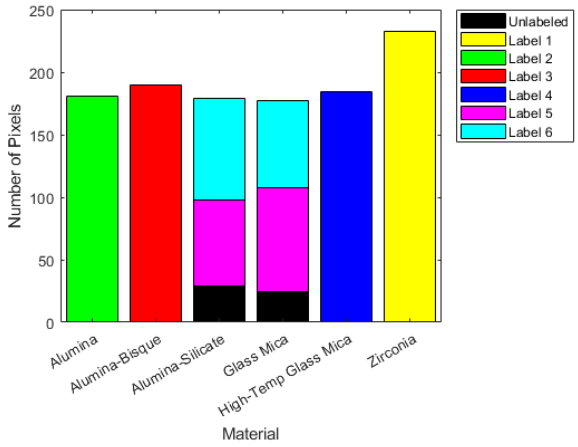

Figure 5.13: Label assignment for each material for iterative hierarchical clustering on the single-channel ceramic cylinders data.

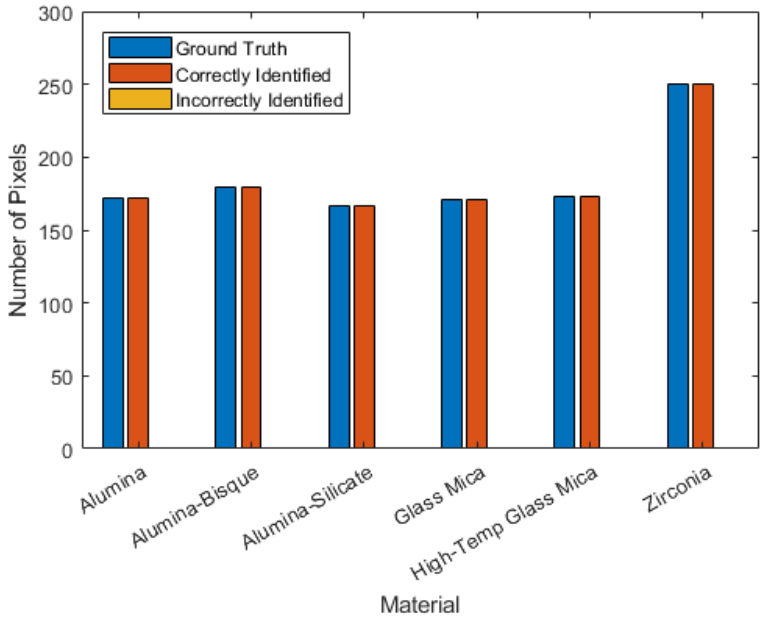

Figure 5.14: Accuracy of material identification with multichannel data.

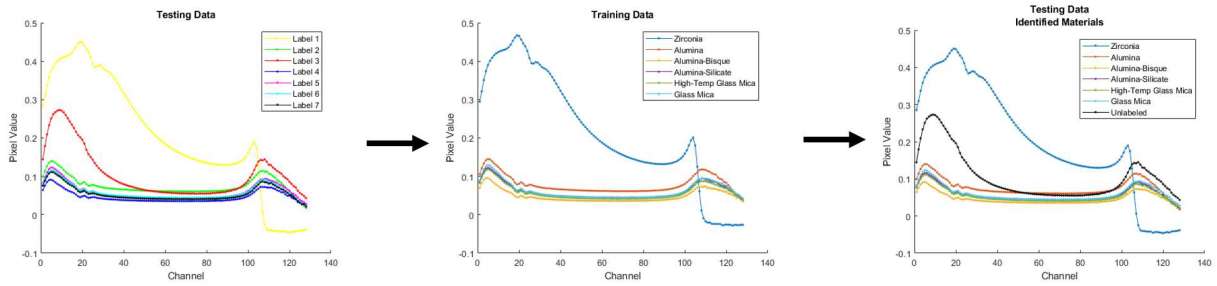

Figure 5.15: Mean profile comparison process.

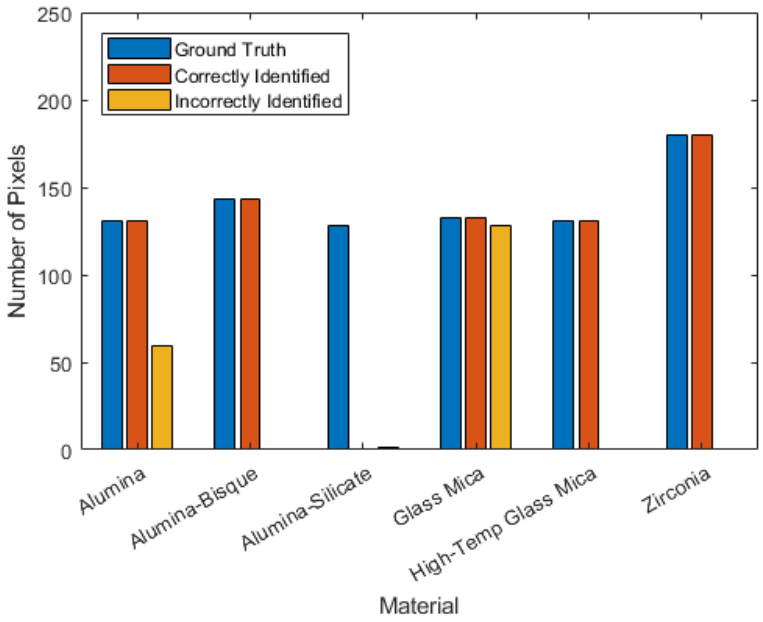

Figure 5.16: Accuracy of material identification with single-channel data.

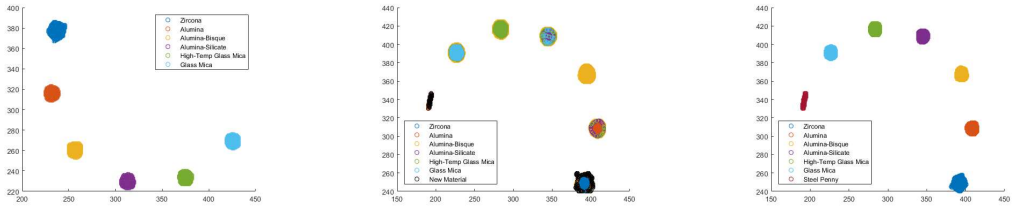

(a) Training data (b) Identified materials in testing data (c) Ground truth for testing data

Figure 5.17: Visualization of training and testing data sets for material inference on raw scan.

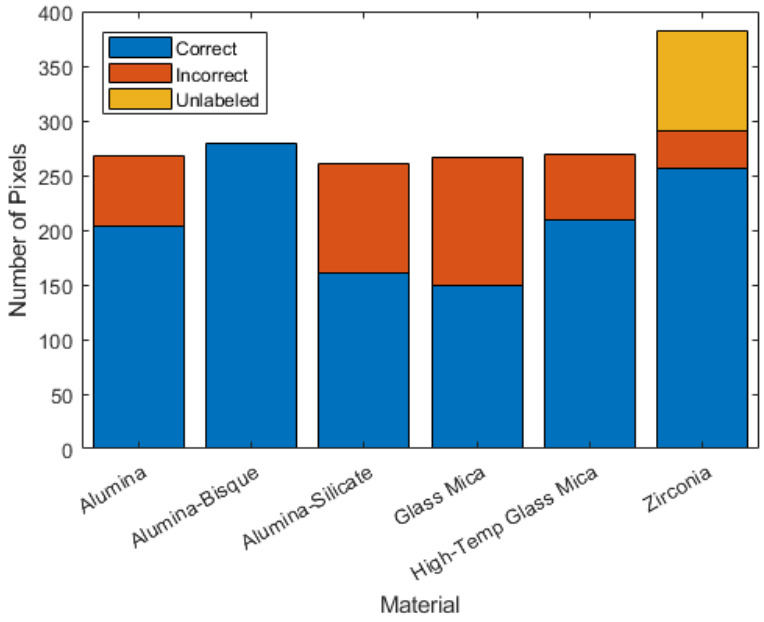

Figure 5.18: Accuracy of material identification with raw scan.

Chapter 6

Publications

1. Jimenez, Edward S., et al. "Non-Destructive Materials Identification System using Spectral Computed Tomography. IEEE Nuclear Science Symposium and Medical Imaging Conference, Nov 2018 (Accepted).

2. Gallegos, Isabel O., et al. Unsupervised Learning Methods to Perform Material Identification Tasks on Hyperspectral Computed Tomography Data. Radiation Detectors in Medicine, Industry, and National Security XIV. International Society for Optics and Photonics, 2018.

3. Koundinyan, Srivathsan P, et al. Machine Learning for Industrial Material Classification Applications with Color CT Datasets. ASNT Research Symposium 2018 (In press).

4. Koundinyan, Srivathsan P., et al., "Supervised Deep Learning Techniques for Material Classification with Spectral Computed Tomography Datasets", QNDE 2018 (In press).

5. Jimenez, Edward S., et al. "Leveraging multi-channel x-ray detector technology to improve quality metrics for industrial and security applications." Radiation Detectors in Medicine, Industry, and National Security XVIII. Vol. 10393. International Society for Optics and Photonics, 2017.

6. Flicker, Celia J., and Edward S. Jimenez. "Optimization of input parameters to improve big-data computed tomography reconstruction performance (Conference Presentation)." Radiation Detectors in Medicine, Industry, and National Security XVIII. Vol. 10393. International Society for Optics and Photonics, 2017.

7. Collins, Noelle, Edward S. Jimenez, and Kyle R. Thompson. "Material identification with multichannel radiographs." AIP Conference Proceedings. Vol. 1806. No. 1. AIP Publishing, 2017.

8. Jimenez, Edward S., et al. "Developing imaging capabilities of multi-channel detectors comparable to traditional x-ray detector technology for industrial and security applications." Radiation Detectors: Systems and Applications XVII. Vol. 9969. International Society for Optics and Photonics, 2016.

Chapter 7

Technology Advances for Patent

1. SD #14601 Machine and Deep learning for Material Identification using Spectral CT
2. SD #13598 Large-Scale Multi-Energy Iterative Volumetric Reconstruction Methods
3. SD #14108 A Program to Acquire and Convert Binary Data from the MultiX Detector
4. SD #14438 cXrayViz: Color X-ray Visualization Tool
5. SD #14436 The Polychromatic X-ray Computed Tomography and Radiography Acquisition system
6. SD #14793 Unsupervised Learning Methods to Perform Material Identification Tasks
7. SD #14797 A Simulation Tool for Parallel- Beam Spectral Radiography Using PHITS
8. SD #14796 MCNP and PHITS Automated Rotation Input Files Generator

Chapter 8

Team Members

Team members on this project over the course of 3 years include:

1. Edward S. Jimenez
2. Kyle R. Thompson
3. Srivathsan Koundinyan
4. Elizabeth Lopez
5. Ryan N. Goodner
6. Isabel O. Gallegos
7. Gabriella M. D. Dalton
8. Christine Mennicke
9. Julia A. Sakamoto
10. Noelle M. Collins
11. Erica A. Holswade
12. Madison L. Devonshire
13. Celia J. Flicker
14. April N. Suknot
15. Samuel S. Fayad
16. John Korbin
17. Stephen Attaway
18. Burke L. Kernen
19. Andrew Lentfer

20. Carl L. Jacques
21. Enrico Quintana
22. Collin Epstein
23. Adriana Stohn
24. Tina Tran

References

[1] Matlab multithresh, 2017b. The MathWorks, Natick, MA.

[2] Harrison H. Barrett and Kyle J. Myers. *Foundations of Image Science*. Wiley-Interscience, 2004.

[3] P. Berkhin. A survey of clustering data mining techniques. In Jacob Kogan, Charles Nicholas, and Marc Teboulle, editors, *Grouping Multidimensional Data: Recent Advances in Clustering*, pages 25–71. Springer Berlin Heidelberg, Berlin, Heidelberg, 2006.

[4] Glen M Blake and Ignac Fogelman. Technical principles of dual energy x-ray absorptiometry. In *Seminars in nuclear medicine*, volume 27, pages 210–228. Elsevier, 1997.

[5] F Edward Boas and Dominik Fleischmann. Evaluation of two iterative techniques for reducing metal artifacts in computed tomography. *Radiology*, 259(3):894–902, 2011.

[6] Keh-Shih Chuang, Hong-Long Tzeng, Sharon Chen, Jay Wu, and Tzong-Jer Chen. Fuzzy c-means clustering with spatial information for image segmentation. *Computerized Medical Imaging and Graphics*, 30:9–15, 2006.

[7] Noelle M. Collins, Kyle R. Thompson, and Edward S. Jimenez. An experiment for material classifications using multichannel radiographs. In *Review of Progress in Quantitative Nondestructive Evaluation*, Jul. 2016.

[8] Chen Deyun, Li Zhiqiang, Gao Ming, Wang Lili, and Yu Xiaoyang. A superresolution image reconstruction algorithm based on landweber in electrical capacitance tomography. *Mathematical Problems in Engineering*, 2013, 2013.

[9] Thomas G Dietterich and Ghulum Bakiri. Solving multiclass learning problems via error-correcting output codes. *Journal of artificial intelligence research*, 2:263–286, 1994.

[10] Huanjun Ding and Sabee Molloi. Image-based spectral distortion correction for photon-counting x-ray detectors. *Medical physics*, 39(4):1864–1876, 2012.

[11] Mohammed T. H. Elbatta and Wesam M. Ashour. A dynamic method for discovering density varied clusters. *International Journal of Signal Processing, Image Processing and Pattern Recognition*, 6:123–134, 2013.

[12] Martin Ester, Hans-Peter Kriegel, Jorg Sander, and Xiaowei Xu. A density-based algorithm for discovering clusters a density-based algorithm for discovering clusters in large spatial databases with noise. In Evangelos Simoudis, Jiawei Hanand, and Usama Fayyad, editors, *Proceedings of the Second International Conference on Knowledge Discovery and Data Mining*, KDD'96, pages 226–231, 1996.

[13] L.A. Feldkamp, L.C. Davis, and J.W. Kress. Practical cone-beam algorithm. *Journal of the Optical Society of America A*, 1(6):612–619, 1984.

[14] Thomas E Hartman. Dual-energy radiography. In *Seminars in roentgenology*, volume 32, pages 45–49. Elsevier, 1997.

[15] James Hunter. Dual Energy Beam Hardening Correction for Inudstrial X-Ray Computed Tomography. Master's thesis, New Mexico Institute of Mining and Technology, United States, 2007.

[16] Jasmine Irani, Nitin Pise, and Madhura Phatak. Clustering techniques and the similarity measures used in clustering: A survey. *International Journal of Computer Applications*, 134:9–14, 2016.

[17] Anil K. Jain. Data clustering: 50 years beyond k-means. *Pattern Recognition Letters*, 31:651–666, 2010.

[18] Zexuan Ji, Yong Xia, Qiang Chen, Quansen Sun, Deshen Xia, and David Dagan Feng. Fuzzy c-means clustering with weighted image patch for image segmentation. *Applied Soft Computing*, 12:1659–1667, 2012.

[19] Edward S. Jimenez. *Simulation and Estimation of Organ Uptake in a Digital Mouse Phantom*. PhD thesis, The University of Arizona, 2010.

[20] Edward S Jimenez, Noelle M Collins, Erica A Holswade, Madison L Devonshire, and Kyle R Thompson. Comparing imaging capabilities of multi-channel detectors to traditional x-ray detecto technology for industrial and security applications. In *SPIE Optical Engineering+ Applications*. International Society for Optics and Photonics, 2016.

[21] Edward S Jimenez and Laurel J Orr. Rethinking the union of computed tomography reconstruction and gpgpu computing. In *Penetrating Radiation Systems and Applications XIV*, volume 8854, page 88540A. International Society for Optics and Photonics, 2013.

[22] Edward S. Jimenez, Laurel J. Orr, Megan L. Morgan, and Kyle R. Thompson. Exploring mediated reality to approximate x-ray attenuation coefficients from radiographs. In *Penetrating Radiation Systems and Applications XIV at SPIE Optics+Photonics 2014*, Aug. 2014.

[23] Edward S. Jimenez, Laurel J. Orr, and Kyle R. Thompson. An Irregular Approach to Large-Scale Computed Tomography on Multiple Graphics Processors Improves Voxel Processing Throughput. In *Workshop on Irregular Applications: Architectures and Algorithms*, The International Conference for High Performance Computing, Networking, Storage and Analysis, November 2012.

[24] Edward S. Jimenez, Laurel J. Orr, and Kyle R. Thompson. Object composition identification via mediated-reality supplemented radiographs. In *IEEE Nuclear Science Symposium and Medical Imaging Conference*, Nov. 2014.

[25] Edward S Jimenez, Laurel J Orr, Kyle R Thompson, and Ryeojin Park. A high-performance and energy-efficient ct reconstruction algorithm for multi-terabyte datasets. In *Nuclear Science Symposium and Medical Imaging Conference (NSS/MIC), 2013 IEEE*, pages 1–7. IEEE, 2013.

[26] Edward S Jimenez and Kyle R Thompson. exploring the existence of null spaces in mediated-reality supplemented methods to x-ray attenuation estimation. In *ASNT 24th Research Symposium 2015*, pages 49–53, 2015.

[27] Edward S. Jimenez, Kyle R. Thompson, and Laurel J. Orr. Utilization of virtualized environments for efficient x-ray attenuation approximation. In *ASNT Research Symposium*, Mar. 2014.

[28] Edward S Jimenez, Kyle R Thompson, Adriana Stohn, and Ryan N Goodner. Leveraging multi-channel x-ray detector technology to improve quality metrics for industrial and security applications. In *Radiation Detectors in Medicine, Industry, and National Security XVIII*, volume 10393, page 103930G. International Society for Optics and Photonics, 2017.

[29] Paul C Johns and Martin J Yaffe. X-ray characterisation of normal and neoplastic breast tissues. *Physics in medicine and biology*, 32(6):675, 1987.

[30] Srivathsan P. Koundinyan, April Suknot, and Edward S. Jimenez. Machine learning for industrial material classification applications with color ct datasets. 2018.

[31] Richard DR Macdonald. Design and implementation of a dual-energy x-ray imaging system for organic material detection in an airport security application. In *Machine Vision Applications in Industrial Inspection IX*, volume 4301, pages 31–42. International Society for Optics and Photonics, 2001.

[32] Laurel J Orr, Edward S Jimenez, and Kyle R Thompson. Cluster-based approach to a multi-gpu ct reconstruction algorithm. In *Nuclear Science Symposium and Medical Imaging Conference (NSS/MIC), 2014 IEEE*, pages 1–7. IEEE, 2014.

[33] N. Otsu. A threshold selection method from gray-level histograms. *IEEE Transactions on Systems, Man, and Cybernetics*, 9:62–66, 1979.

[34] Lance Parsons, Ehtesham Haque, and Huan Liu. Subspace clustering for high dimensional data: A review. *SIGKDD Explorations Newsletter*, 6:90–105, 2004.

[35] Ismael Perez, Matthew Bauerle, Edward S Jimenez, and Kyle R Thompson. A high-performance gpu-based forward-projection model for computed tomography applications. In *SPIE Optical Engineering+ Applications*, pages 92150A–92150A. International Society for Optics and Photonics, 2014.

[36] AN Primak, JC Ramirez Giraldo, X Liu, Lifeng Yu, and Cynthia H McCollough. Improved dual-energy material discrimination for dual-source ct by means of additional spectral filtration. *Medical physics*, 36(4):1359–1369, 2009.

[37] E Roessl and R Proksa. K-edge imaging in x-ray computed tomography using multi-bin photon counting detectors. *Physics in medicine and biology*, 52(15):4679, 2007.

[38] Xiaolan Wang, Xin He, Katsuyuki Taguchi, Bradley E Patt, Douglas J Wagenaar, and Eric C Frey. Uniformity correction in photon-counting x-ray detector based on basis material decomposition. In *Nuclear Science Symposium Conference Record, 2008. NSS'08. IEEE*, pages 4902–4905. IEEE, 2008.

[39] Ron Wurtz, Sean Walston, Dan Dietrich, and Harry Martz. Metrics for developing an endorsed set of radiographic threat surrogates for jinii/caars. Technical report, Lawrence Livermore National Laboratory (LLNL), Livermore, CA, 2009.

DISTRIBUTION:

	MS	,
		,
1	MS 0161	Legal Intellectual Property, 11500
1	MS 0899	Technical Library, 9536 (electronic copy)


Sandia National Laboratories